Electronic Supporting Information (ESI)

Trivalent Metal Ion Sensor: Enabled Bioimaging and Quantification of Vaccine Deposited Al^{3+} at Lysosomes

Kavyashree P.,[1#] Ajmal Roshan Unniram Parambil,[1,2,3#] Akshay Silswal,[1] Anup Pramanik,[4] and Apurba Lal Koner [a]*

[1] Bionanotechnology Lab, Department of Chemistry, Indian Institute of Science Education and Research Bhopal, Bhopal Bypass Road, Bhauri, 462066 Bhopal, Madhya Pradesh, India, E-mail: akoner@iiserb.ac.in

[2] Current address: Department of Chemistry, University of Basel, 4058 Basel, Switzerland.

[3] Current address: Institute of Chemistry and Bioanalytics, School of Life Sciences, University of Applied Sciences and Arts Northwestern Switzerland, 4132 Muttenz, Switzerland

[4] Department of Chemistry, Sidho-Kanho-Birsha University, Purulia-723104, West Bengal, India.

[#] Contributed equally

Table of contents

4. NMR titration studies with Al^{3+}

5. Live-cell imaging studies

1. Design and synthesis of probes:

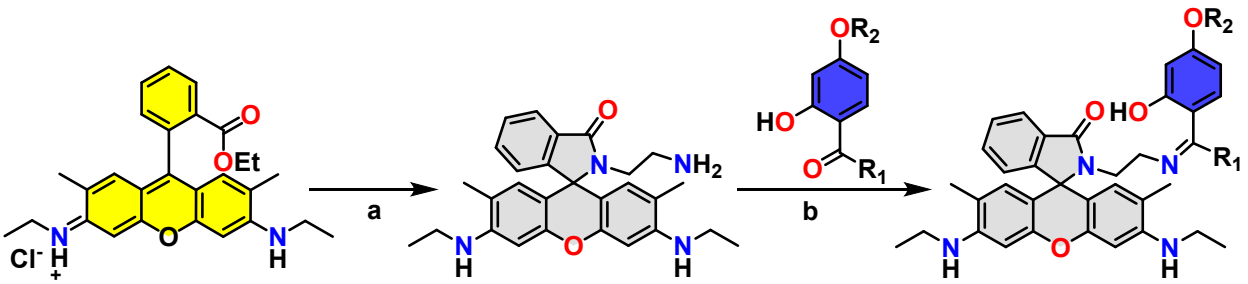

(a) Ethylenediamine, methanol, reflux, overnight, 82 %, (b) Methanol, reflux, 12 h, 34-60 %

Where, Rh-A : R_1=Me, R_2=H, Rh-B : R_1=H, R_2=H, Rh-A-Mor : R_1=Me, R_2=

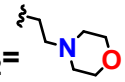

Scheme S1. Synthetic scheme for designed probes

1.1. Synthesis of 2-(2-aminoethyl)-3',6'-bis(ethylamino)-2',7'-dimethylspiro[isoindoline-1,9'-xanthen]-3-one (Rh): [1]

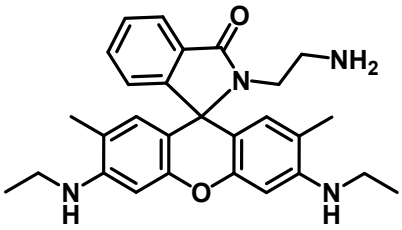

Rhodamine 6G (1.0 g, 2.08 mmol, 1 equiv.) was dissolved in 20 mL of methanol, followed by dropwise addition of ethylenediamine (0.7 mL, 10.44 mmol, 5 equiv.) at room temperature with vigorous stirring. The reaction mixture was refluxed overnight at 60-65 °C until the fluorescence of the mixture disappeared. The pale-pink precipitate formed was filtered, washed with cold ethanol, and dried over vacuum. Yield: 782.8 mg, 82.1%. ^{1}H NMR (500 MHz, $CDCl_3$) δ 7.95 – 7.90 (m, 1H), 7.46 (m, 2H), 7.07 – 7.04 (m, 1H), 6.34 (s, 2H), 6.22 (s, 2H), 3.50 (dd, J = 9.2, 4.2 Hz, 2H), 3.20 (m, 6H), 2.38 (t, J = 6.6 Hz, 2H), 1.90 (s, 6H), 1.33 (t, J = 7.1, 3.1 Hz, 6H). ESI-MS: calculated mass = 456.2525 Da, obtained mass = 457.2588 Da $[M+H]^+$.

1.2. Synthesis of 1-(2-hydroxy-4-(2-morpholinoethoxy)phenyl)ethan-1-one (A-Mor):[2]

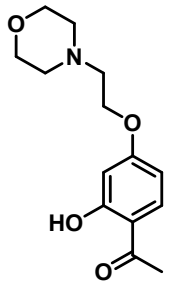

2′,4′-Dihydroxyacetophenone (200 mg, 1.32 mmol, 1 equiv.) was dissolved in 8 mL of dry 2-butanone. Activated potassium carbonate (211 mg, 1.52 mmol, 1.15 equiv.), potassium hydroxide (56 mg, 1.41 mmol, 1.07 equiv.) and 4-(2-Chloroethyl)morpholine hydrochloride (245 mg, 1.32 mmol, 1 equiv.) were added successively with vigorous stirring at room temperature. The reaction mixture was refluxed for 12 hours at 100 °C under inert atmosphere until the TLC revealed the completion of the reaction. The solvent was evaporated under reduced pressure and the solid obtained was dissolved in excess water. The mixture was further extracted with dichloromethane and brine solution, organic layer was collected, dried over anhydrous sodium sulphate and concentrated. Finally, the residue was purified by column chromatography (70% ethyl acetate: hexane) yielding a white crystalline solid. Yield: 160 mg, 45.7%. ^{1}H NMR (500 MHz, $CDCl_3$) δ 12.71 (s, 1H), 7.61 (d, J = 8.9 Hz, 1H), 6.43 (dd, J = 8.9, 2.5 Hz, 1H), 6.39 (d, J = 2.46 Hz, 1H), 4.13 (t, J = 5.7 Hz, 2H), 3.72 (t, J = 4.7 Hz, 4H), 2.80 (t, J = 5.7 Hz, 2H), 2.63 – 2.50 (m, 7H). ESI-MS: calculated mass = 265.1314 Da, Obtained mass = 266.1375 Da $[M+H]^+$

1.3. Synthesis of Rhodamine-based Schiff bases:

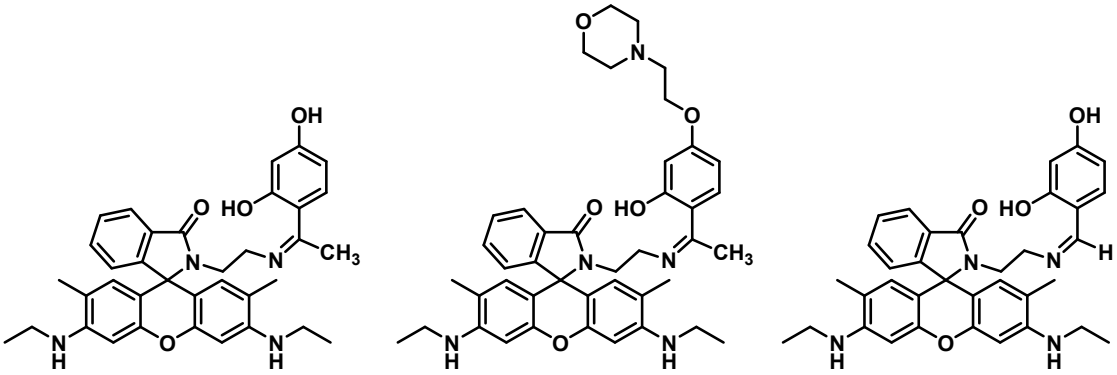

Rh-A Rh-A-Mor Rh-B

Rh (200 mg, 0.44 mmol, 1 equiv.) was suspended in 10 mL of dry methanol, followed by the addition of acetophenone/benzaldehyde derivatives (0.44 mmol, 1 equiv.) at room temperature with vigorous stirring. The mixture was refluxed for 12 hours at 70 ℃ under dark conditions keeping an inert atmosphere. The pale-yellow precipitate formed was collected, washed with cold ethanol, and dried over vacuum.

(Z)-2-(2-((1-(2,4-dihydroxyphenyl)ethylidene)amino)ethyl)-3',6'-bis(ethylamino)-2',7'-dimethylspiro[isoindoline-1,9'-xanthen]-3-one (Rh-A): Yield: 90 mg, 34.6%. ^{1}H NMR (500 MHz, DMSO-d_6) δ 15.99 (s, 1H), 9.70 (s, 1H), 7.80 (s, 1H), 7.50 (d, J = 4.5 Hz, 2H), 7.31 (d, J = 8.8 Hz, 1H), 6.98 (d, J = 5.3 Hz, 1H), 6.26 (s, 2H), 6.11 (d, J = 8.4 Hz, 1H), 6.07 (s, 2H), 6.03 (s, 1H), 5.05 (t, J = 5.6 Hz, 2H), 3.15 – 3.05 (m, 6H), 1.89 (s, 3H), 1.75 (s, 6H), 1.20 (t, J = 7.1 Hz, 6H).

^{13}C{^{1}H} NMR (125 MHz, DMSO-*d6*) δ 13.68, 14.21, 16.81, 30.69, 37.42, 63.92, 95.51, 103.25, 103.90, 106.28, 111.60, 118.34, 122.43, 123.58, 127.67, 128.25, 130.10, 130.29, 132.72, 147.68, 150.86, 153.49, 161.35, 166.86, 167.00, 171.93.

ESI-MS: Calculated mass = 590.2893 Da, Obtained mass = 591.2951 Da $[M+H]^+$

(Z)-3',6'-bis(ethylamino)-2-(2-((1-(2-hydroxy-4-(2-morpholinoethoxy)phenyl)ethylidene) amino)ethyl)-2',7'-dimethylspiro[isoindoline-1,9'-xanthen]-3-one (Rh-A-Mor): Yield: 115 mg, 37.9%. ^{1}H NMR (500 MHz, DMSO-d_6) δ 16.12 (s, 1H), 7.80 (dd, J = 5.9, 2.9 Hz, 1H), 7.53 – 7.48 (m, 2H), 7.38 (d, J = 8.8 Hz, 1H), 7.00 – 6.96 (m, 1H), 6.26 (s, 2H), 6.24 – 6.19 (m, 2H), 6.08 (s, 2H), 5.05 (t, J = 5.5 Hz, 2H), 4.04 (t, J = 5.7 Hz, 2H), 3.56 (t, J = 4.6 Hz, 4H), 3.16 – 3.06 (m, 6H), 2.64 (t, J = 5.7 Hz, 2H), 2.44 (t, J = 4.7 Hz, 4H), 1.93 (s, 3H), 1.74 (s, 6H), 1.20 (t, J = 7.1 Hz, 6H).

^{13}C{^{1}H} NMR (125 MHz, DMSO-*d6*) δ14.13, 16.86, 30.68, 37.42, 53.59, 56.88, 63.97, 65.15, 66.22, 95.51, 102.09, 104.56, 104.83, 112.33, 118.24, 122.44, 123.49, 127.67, 128.23, 129.97, 130.32, 132.72, 147.68, 150.86, 153.49, 162.10, 166.96, 167.76, 172.13.

ESI-MS: Calculated mass = 703.3734 Da, Obtained mass = 704.3809 Da $[M+H]^+$

(Z)-2-(2-((2,4-dihydroxybenzylidene)amino)ethyl)-3',6'-bis(ethylamino)-2',7'dimethylspiro [isoindoline-1,9'-xanthen]-3-one (Rh-B): Yield: 150 mg, 59.1%. ^{1}H NMR (500 MHz, DMSO-d_6) δ 13.35 (s, 1H), 9.92 (s, 1H), 7.83 (s, 1H), 7.77 (dd, J = 6.0, 2.5 Hz, 1H), 7.54 – 7.46 (m, 2H), 7.02 (d, J = 8.5 Hz, 1H), 7.00 – 6.96 (m, 1H), 6.27 (s, 2H), 6.22

(dd, J = 8.4, 2.3 Hz, 1H), 6.12 (d, 1H), 6.05 (s, 2H), 5.05 (t, J = 5.4 Hz, 2H), 3.27 (t, J = 6.7 Hz, 2H), 3.17 – 3.07 (m, 6H), 1.81 (s, 6H), 1.21 (t, J = 7.1 Hz, 6H).

$^{13}C\{^{1}H\}$ NMR (125 MHz, DMSO-d6) δ 14.14, 17.03, 37.47, 55.22, 64.11, 95.59, 102.39, 104.72, 106.70, 111.18, 118.32, 122.41, 123.62, 127.62, 128.26, 130.36, 132.72, 133.16, 147.72, 151.03, 153.34, 161.48, 163.86, 165.26, 167.01.

ESI-MS: Calculated mass = 576.2737 Da, Obtained mass = 577.2828 Da $[M+H]^+$

2. NMR and mass data

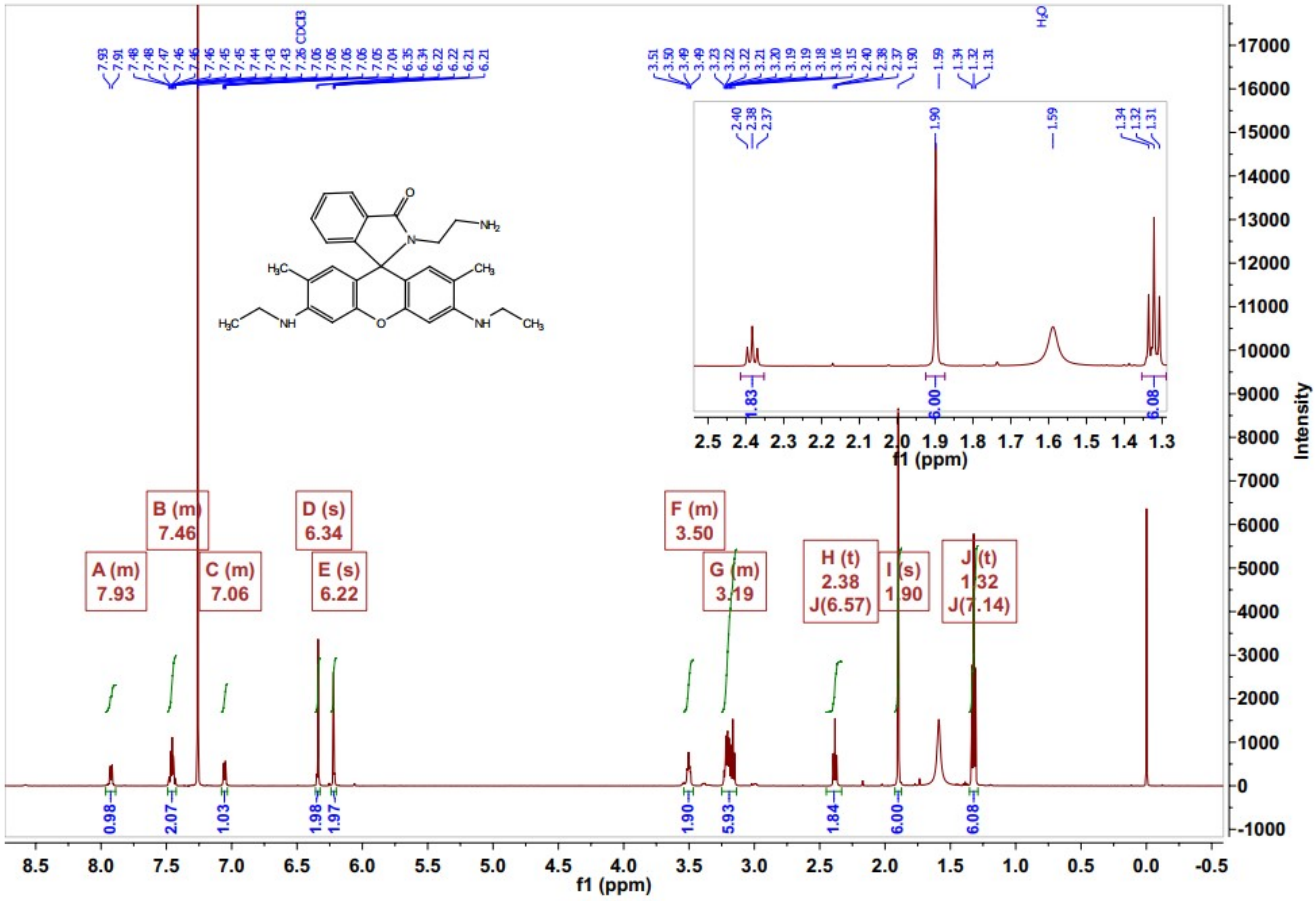

Fig. S1: ^{1}H NMR spectrum for **Rh** recorded in $CDCl_3$ at 500 MHz

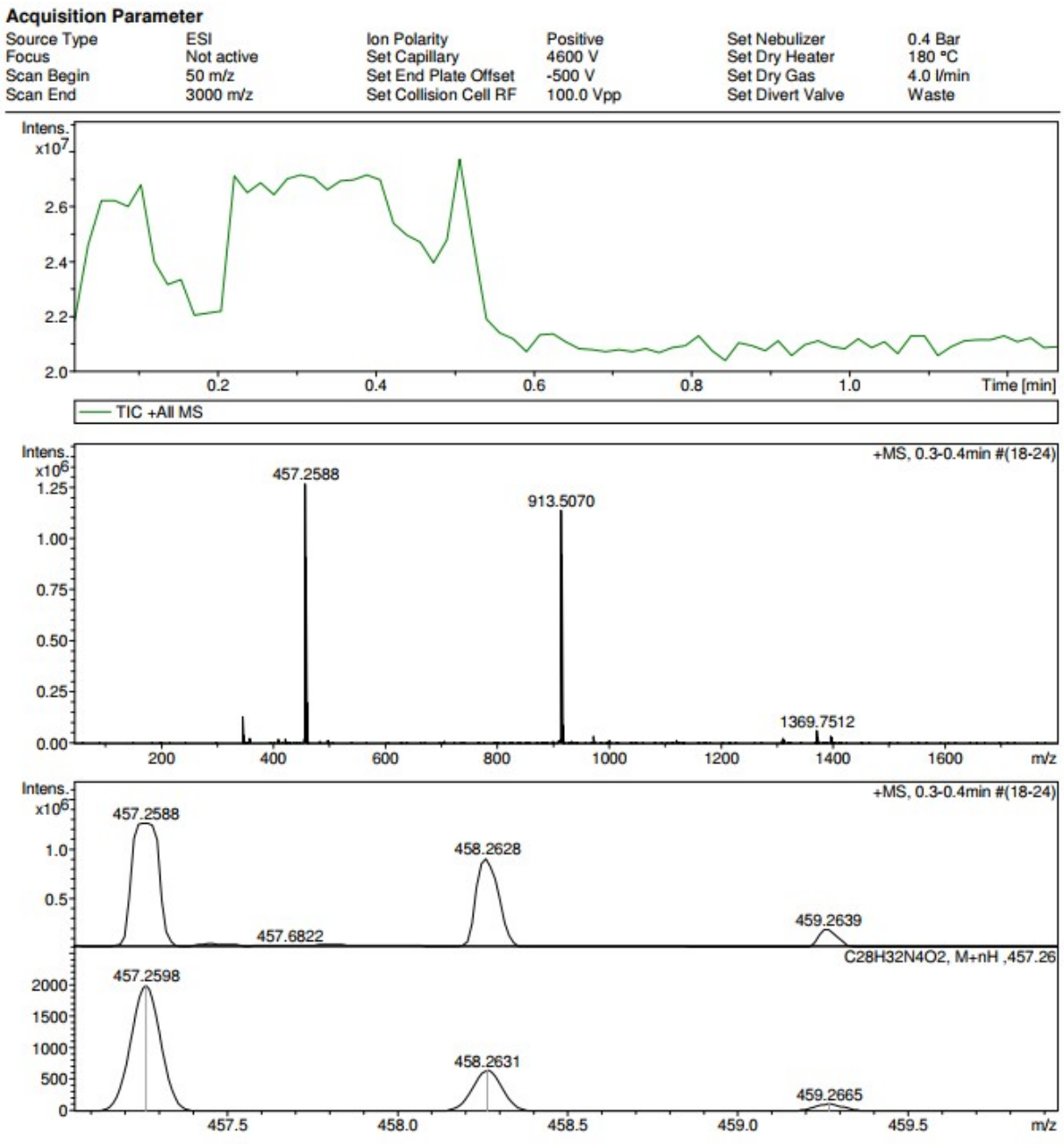

Fig. S2: HRMS for **Rh**; **Calculated mass** = 456.2525 Da, **Obtained mass** = 457.2588 Da $[M+H]^+$

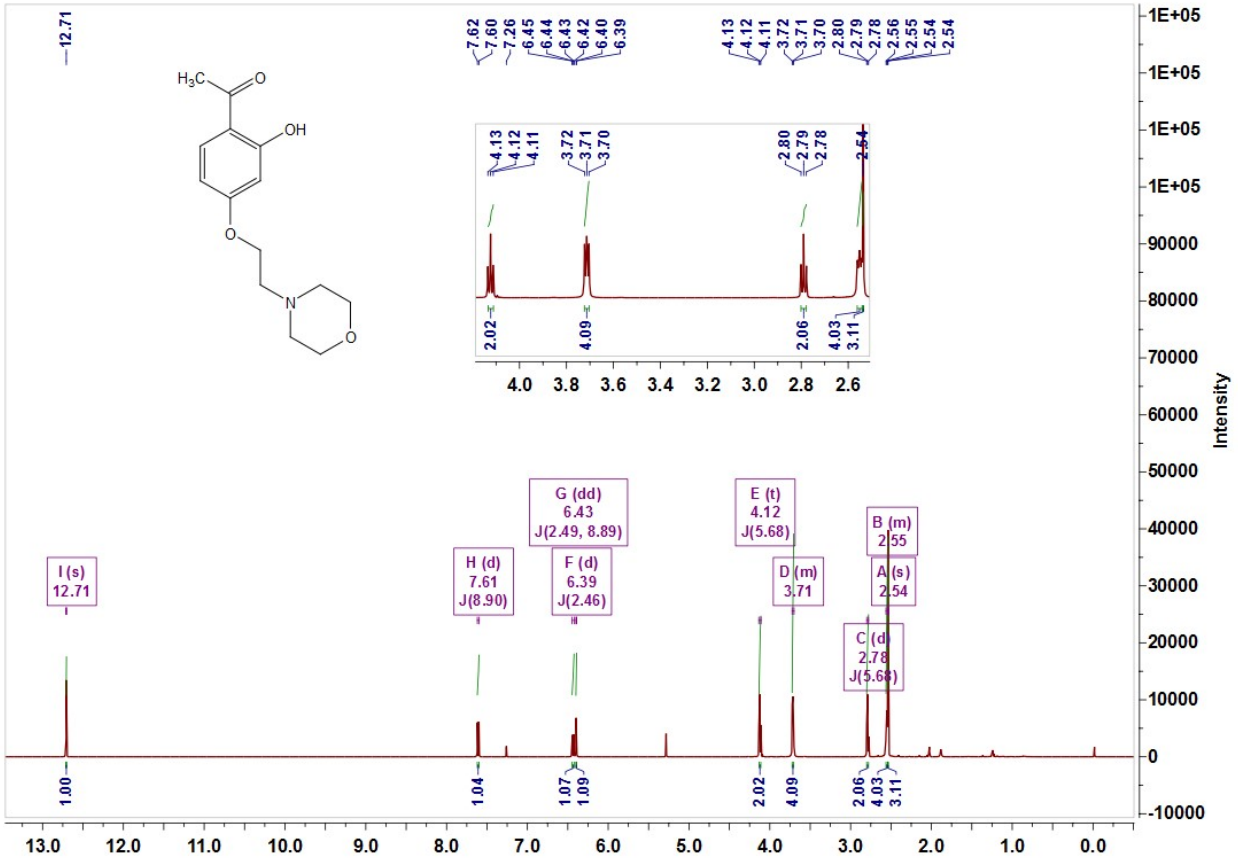

Fig. S3: ^{1}H NMR spectrum for **A-Mor** recorded in $CDCl_3$ at 500 MHz

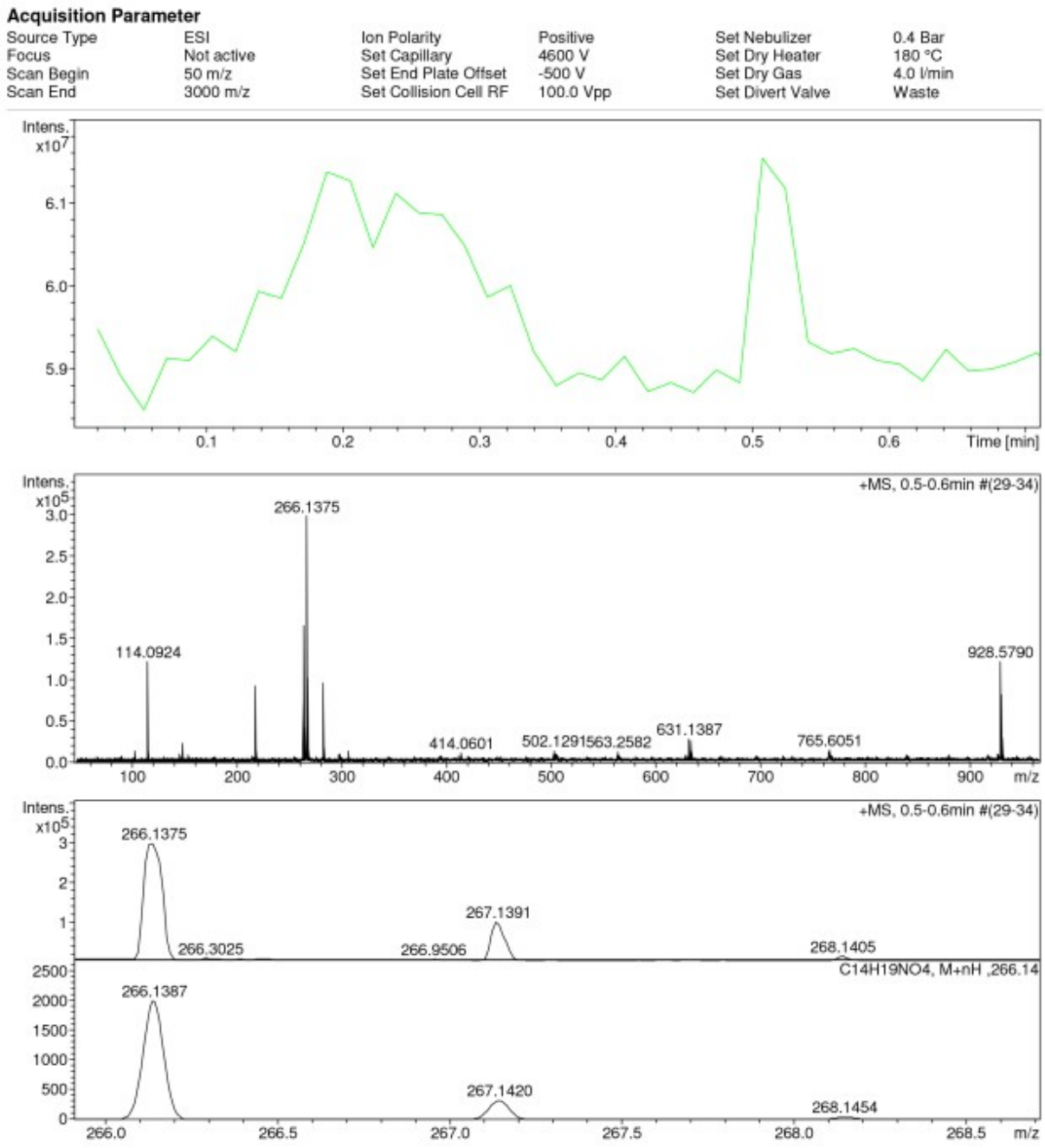

Fig. S4: HRMS for **A-Mor**; **Calculated mass** = 265.1314 Da, **Obtained mass** = 266.1375 Da $[M+H]^+$

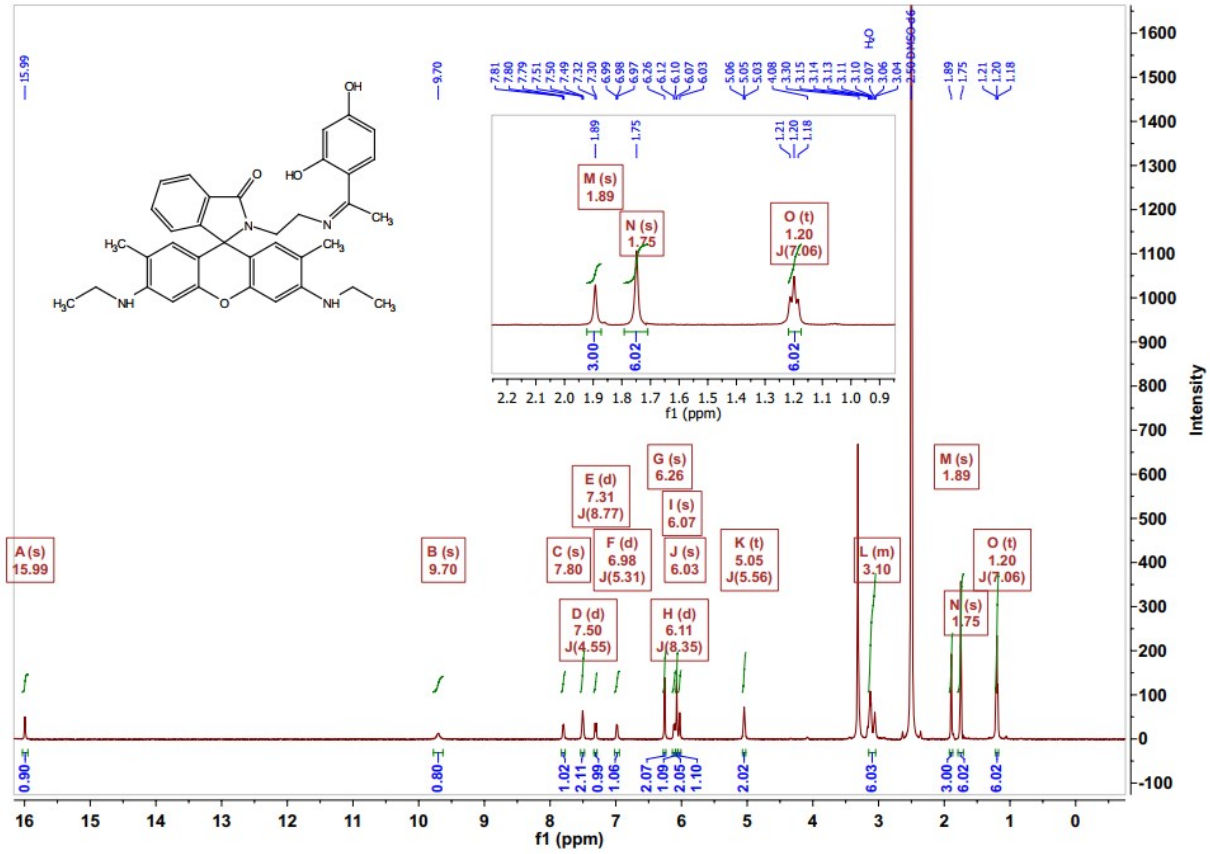

Fig. S5: ^{1}H NMR spectrum of **Rh-A** recorded in DMSO-*d6* at 500 MHz

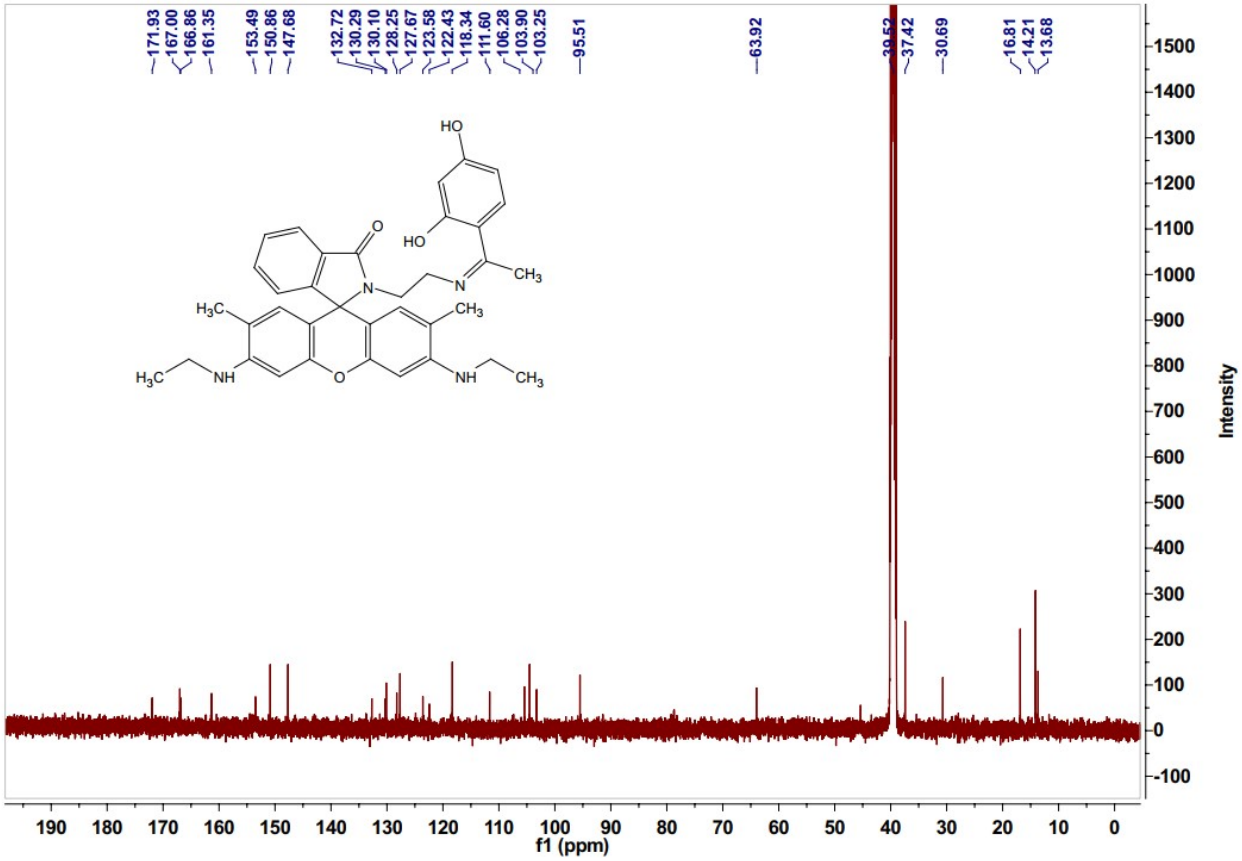

Fig. S6: ^{13}C NMR spectrum for compound **Rh-A** in DMSO-*d6*

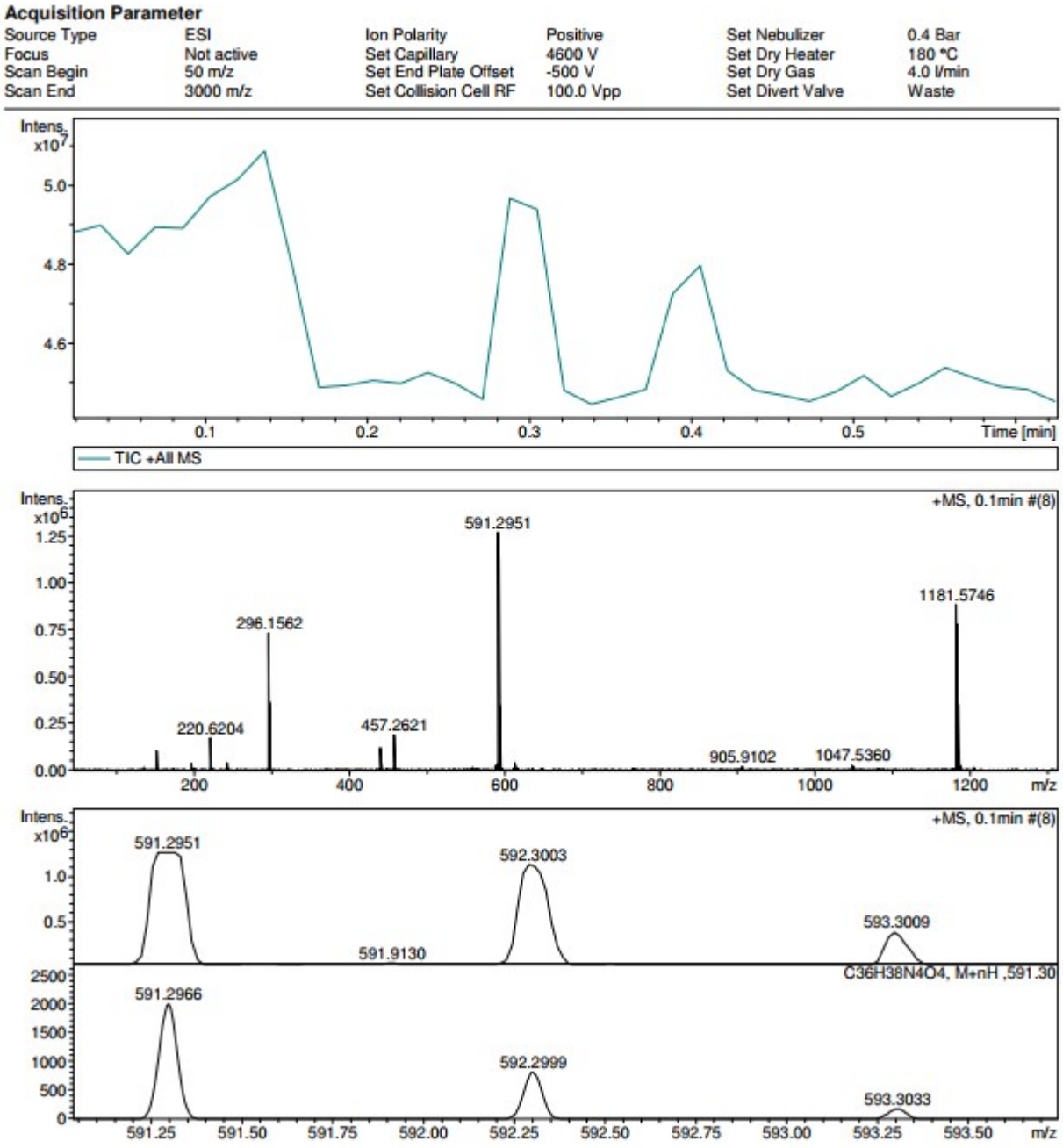

Fig. S7: HRMS for **Rh-A**; **Calculated mass** = 590.2893 Da, **Obtained mass** = 591.2951 Da $[M+H]^+$

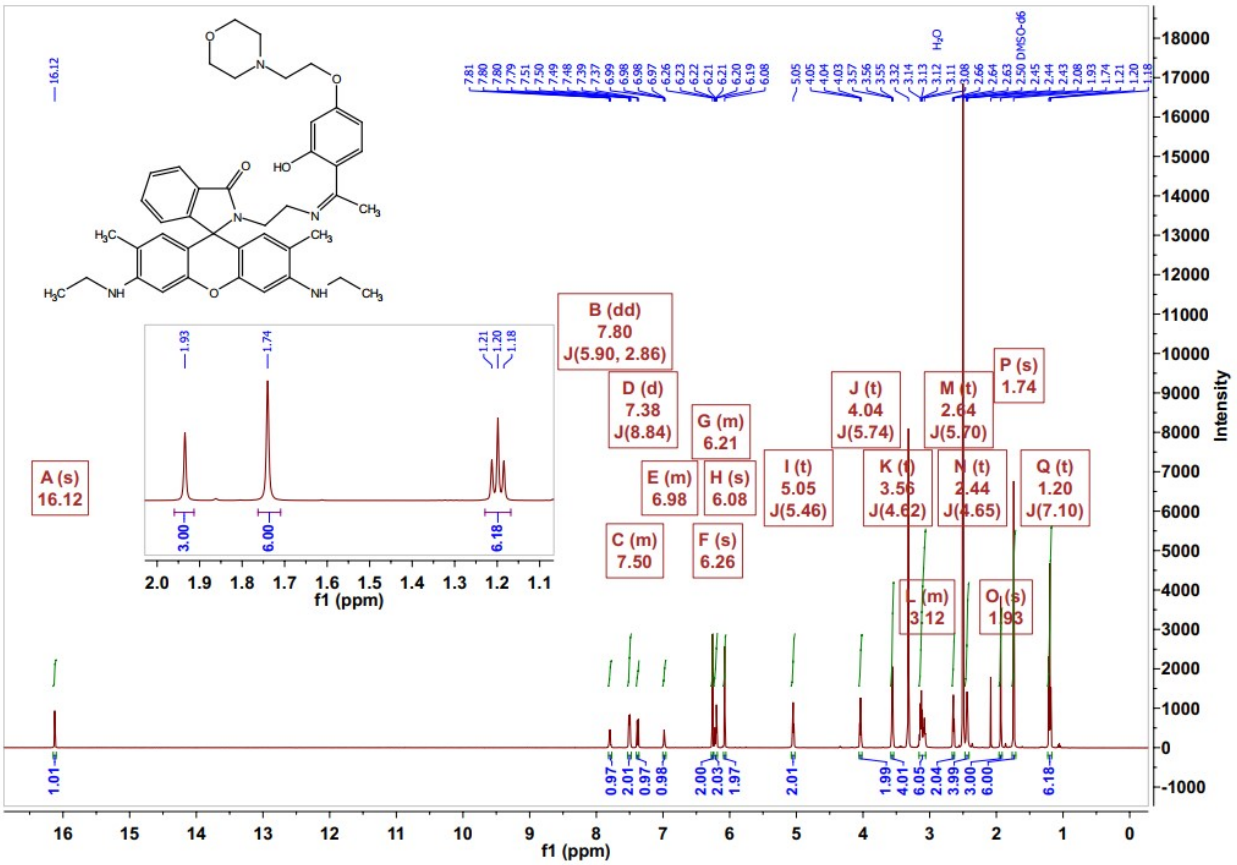

Fig. S8: ^{1}H NMR spectrum of **Rh-A-Mor** recorded in DMSO-*d6*

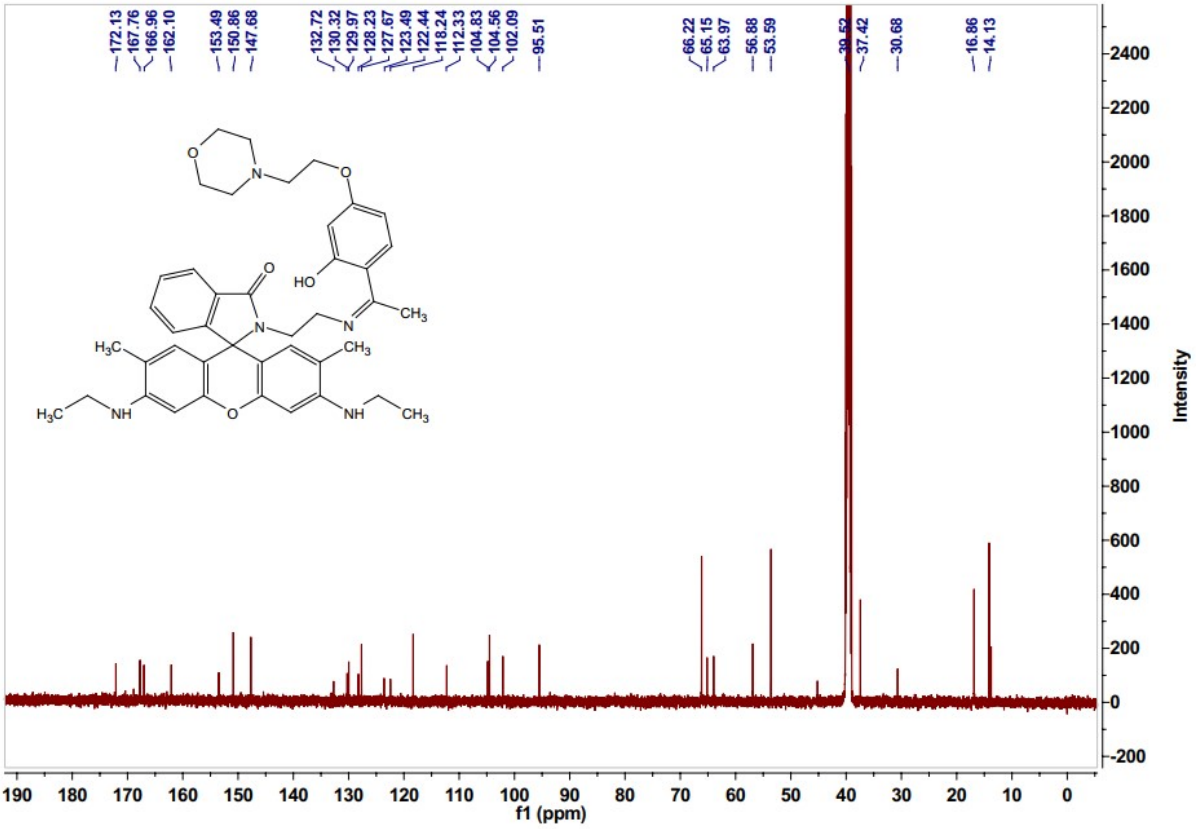

Fig. S9: ^{13}C NMR spectrum for compound **Rh-A-Mor** in DMSO-*d6*

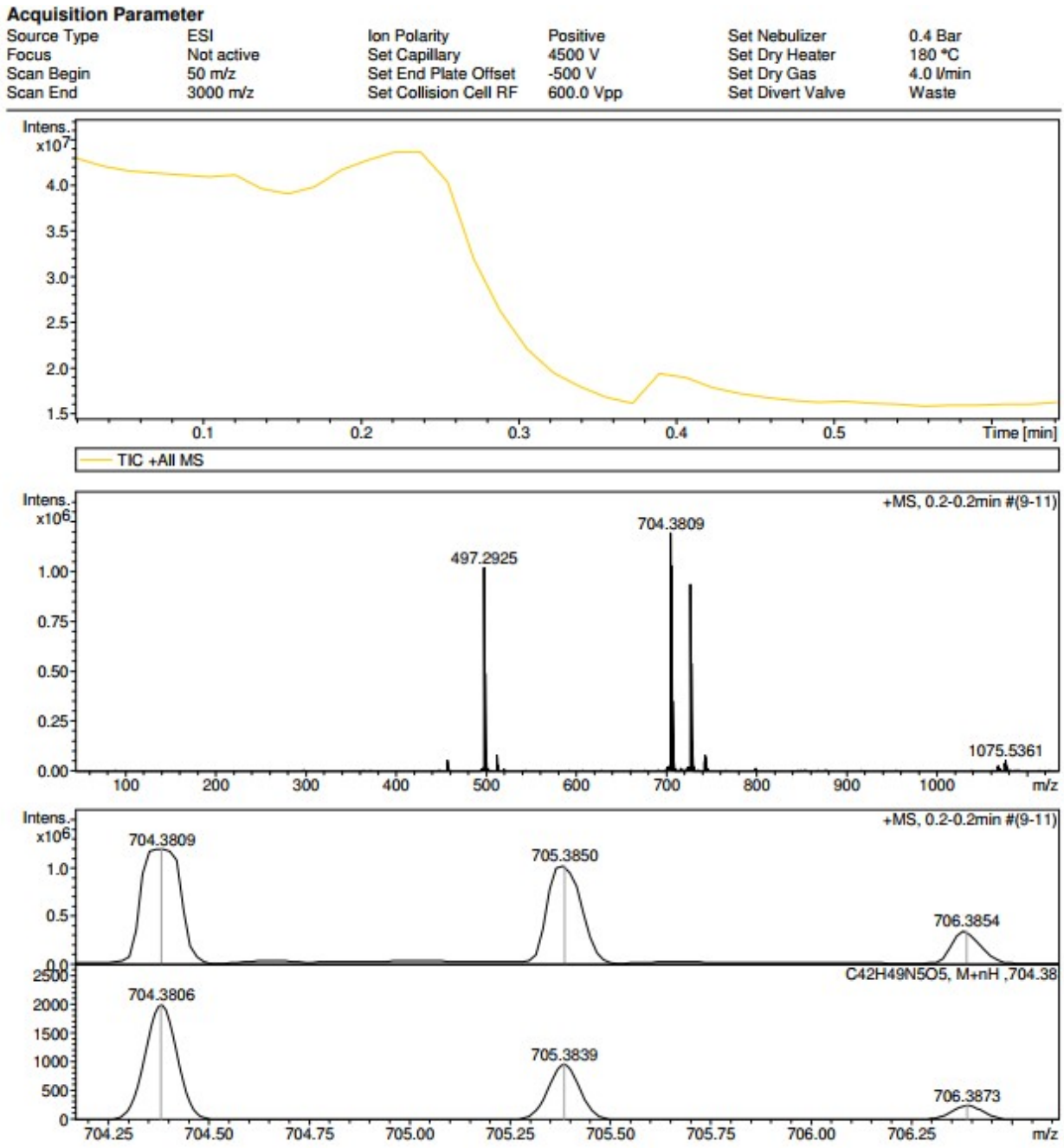

Fig. S10: HRMS for **Rh-A-Mor**; **Calculated mass** = 703.3734 Da, **Obtained mass** = 704.3809 Da $[M+H]^+$

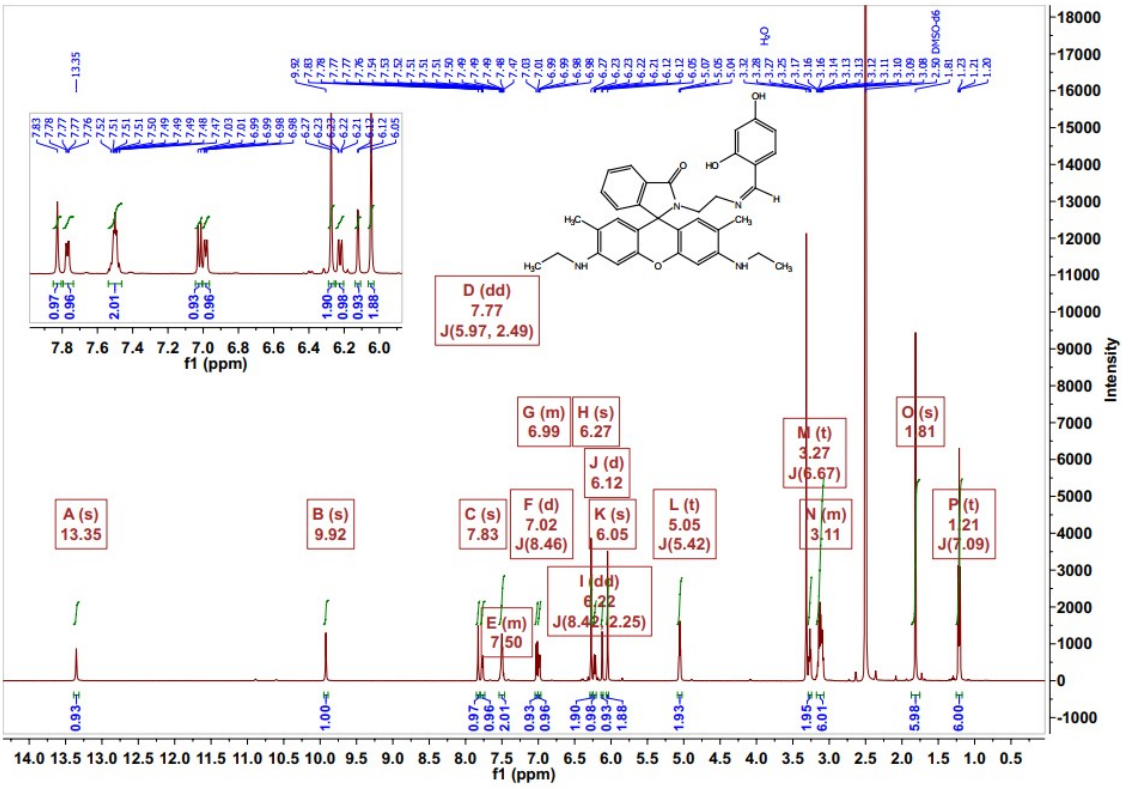

Fig. S11: ^{1}H NMR spectrum of **Rh-B** recorded in DMSO-d_6

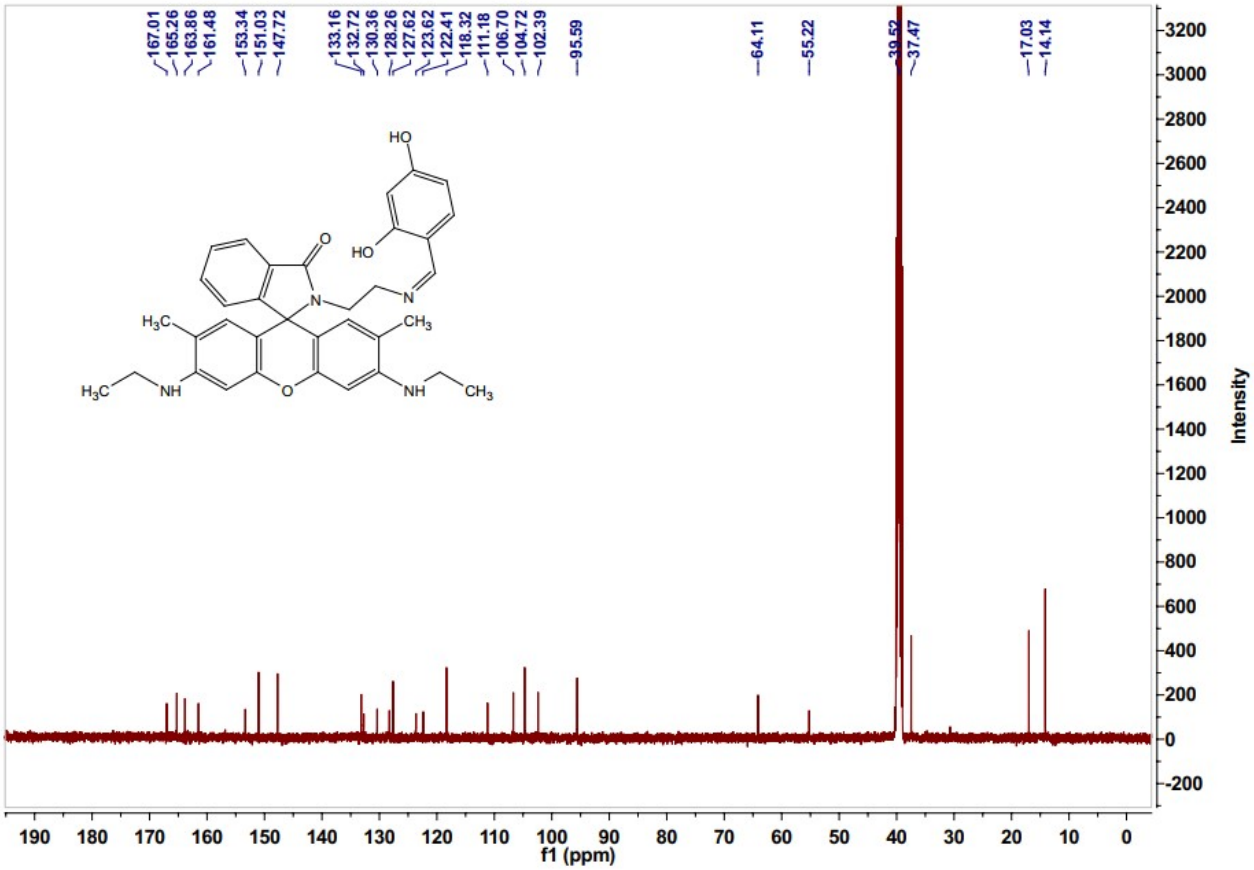

Fig. S12: ^{13}C NMR spectrum for compound **Rh-B** in DMSO-d6

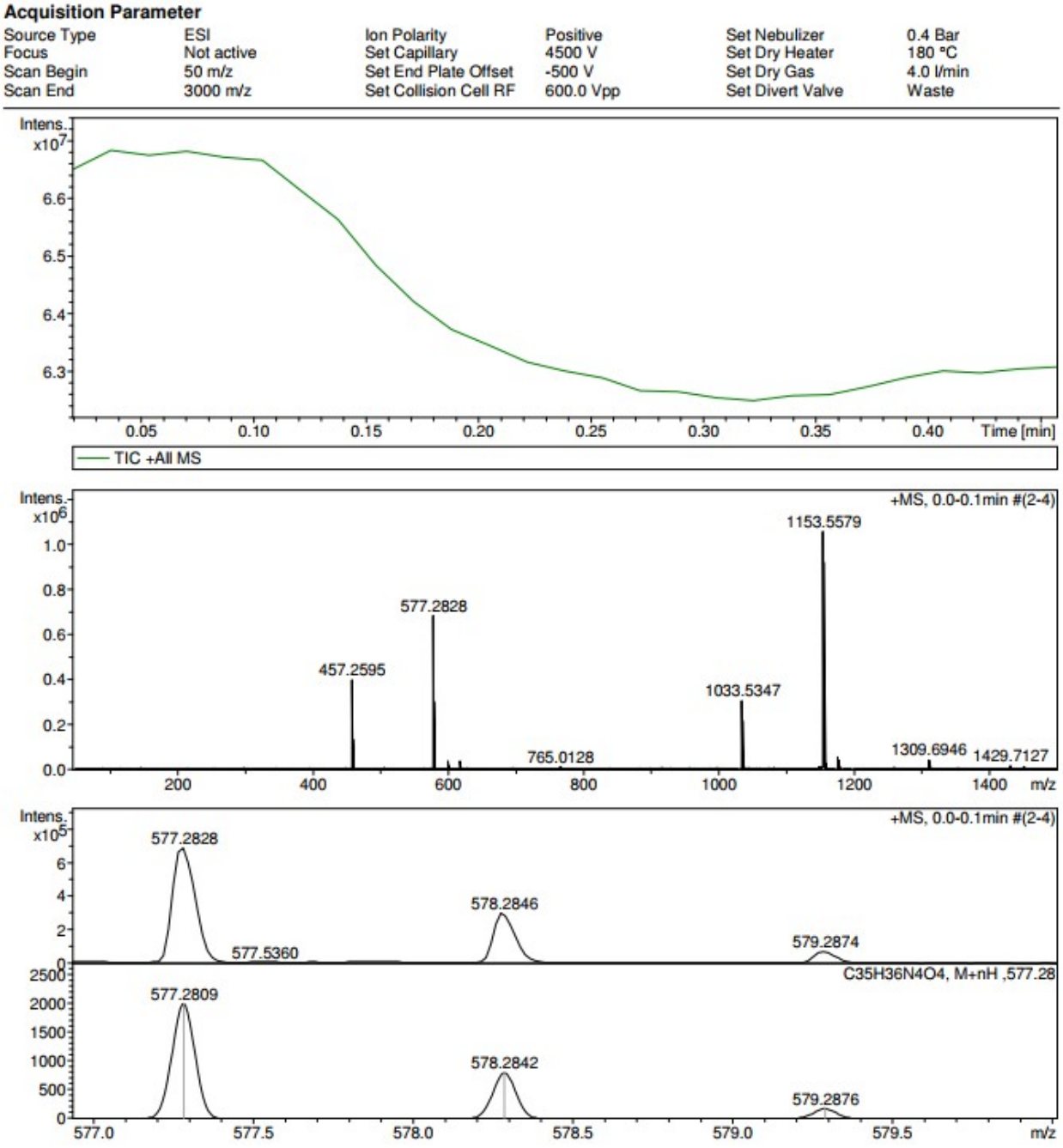

Fig. S13: HRMS for **Rh-B**; **Calculated mass** = 576.2737 Da, **Obtained mass** = 577.2828 Da $[M+H]^+$

3. Spectroscopic studies using Rh-A, Rh-A-Mor, and Rh-B

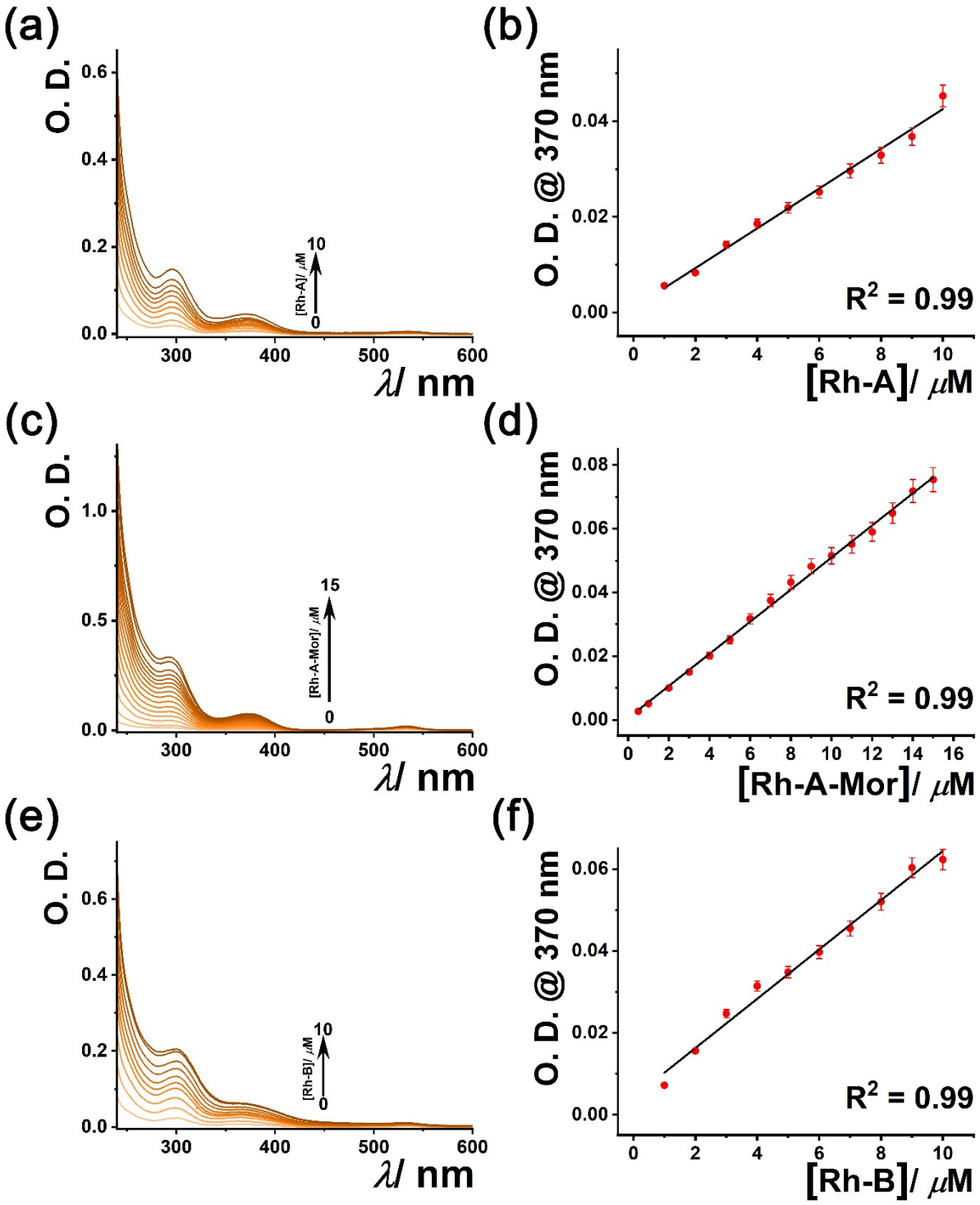

Fig. S14: (a), (c), and (e) are concentration-dependent absorption spectra of **Rh-A, Rh-A-Mor,** and **Rh-B** respectively**,** (b), (d), and (f) are linear plots of abs. max vs. concentration of **Rh-A, Rh-A-Mor,** and **Rh-B** respectively, obeying the Beer-Lambert law, all the experiments are performed in 20 mM NaCl solution in Milli-Q water, pH 6.0, 37 °C.

Table S1: Molar extinction coefficient (ε) of chemosensors at different wavelengths at pH 6.0.

Chemosensor	ε_{294}/ M^{-1} cm^{-1}	ε_{370}/ M^{-1} cm^{-1}
Rh-A	13540	4160
Rh-A-Mor	21860	5040
Rh-B	20310	6020

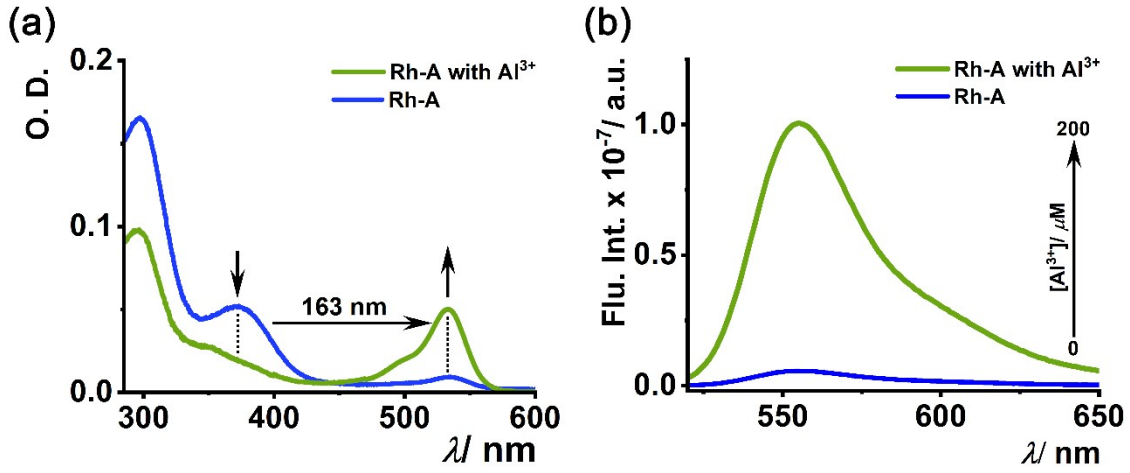

Fig. S15: (a) UV-Vis. absorption and, (b) emission spectra of **Rh-A** in the absence and presence of Al^{3+} (200 μM) in NaCl solution (ionic strength 20 mM, pH 6.0, 37 ℃), [**Rh-A**] = 10 μM, λ_{ex} = 510 nm.

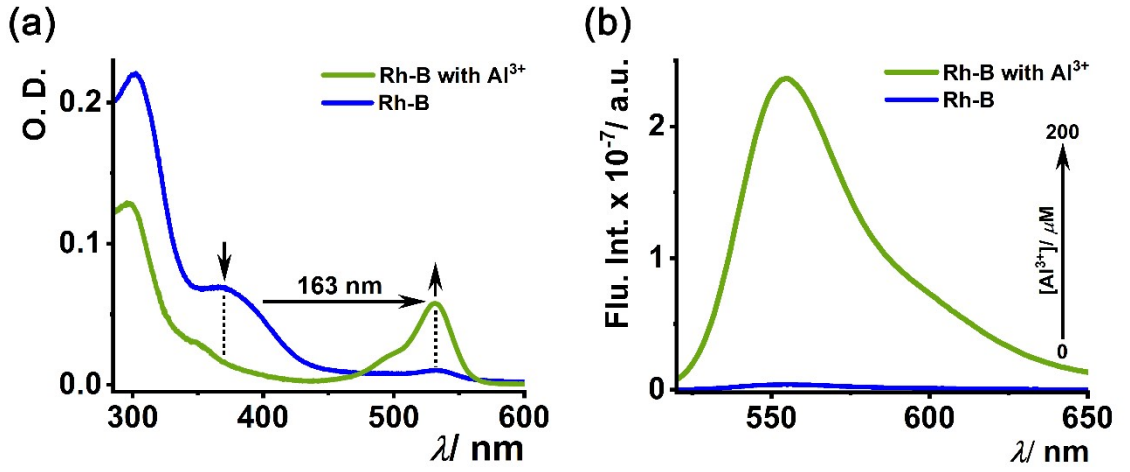

Fig. S16: (a) UV-Vis. absorption and (b) emission spectra of **Rh-B** in the absence and presence of Al^{3+} (200 μM) in NaCl solution (ionic strength 20 mM, pH 6.0, 37 ℃), [**Rh-B**] = 10 μM, λ_{ex} = 510 nm.

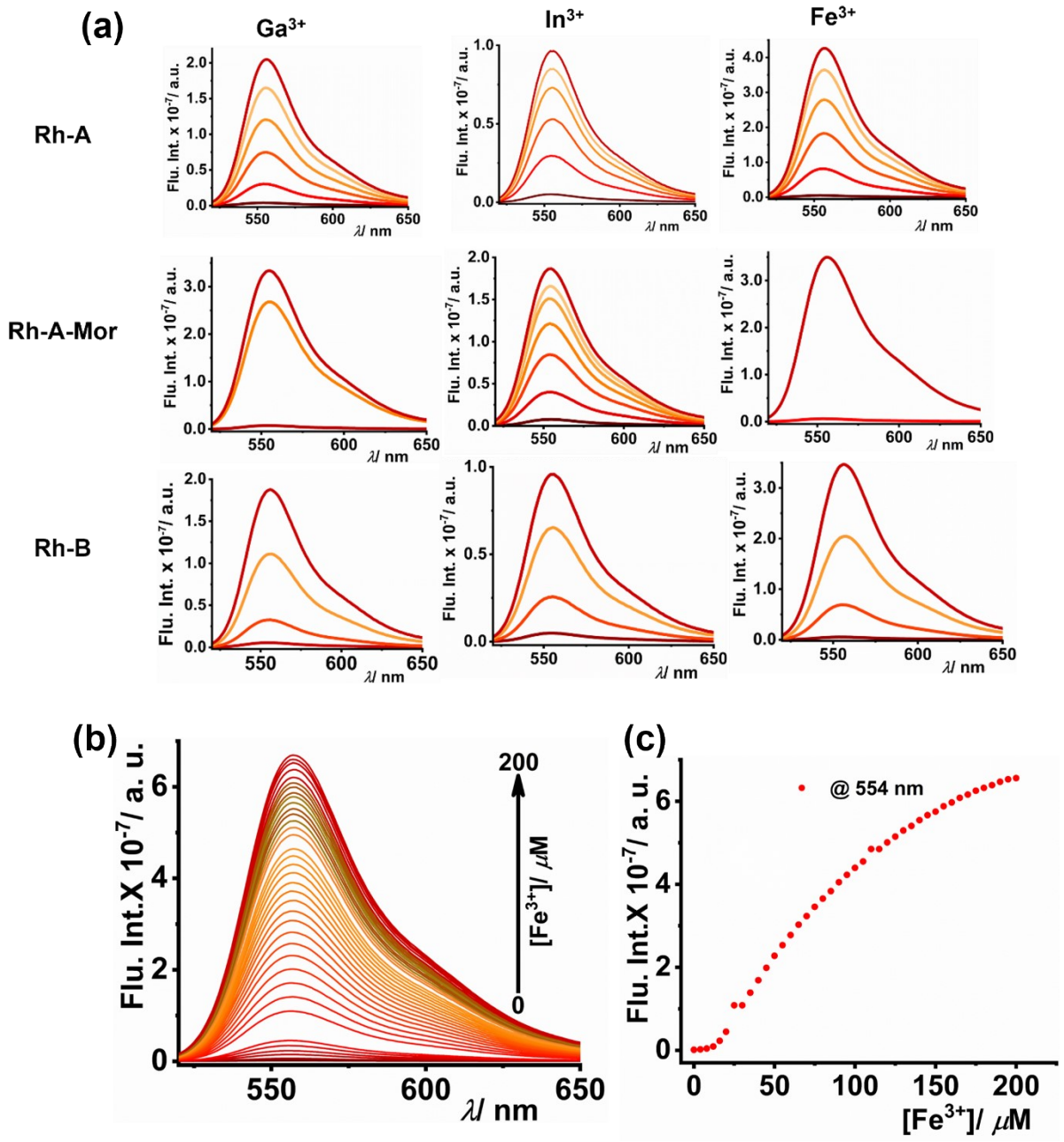

Fig. S17: (a) Emission spectra of Rhodamine derivatives with other trivalent metal ions, (b) emission spectra of **Rh-A-Mor** (5 μM) with different concentrations of Fe^{3+}, (c) plot of fluorescence intensity *vs.* concentration of Fe^{3+}.

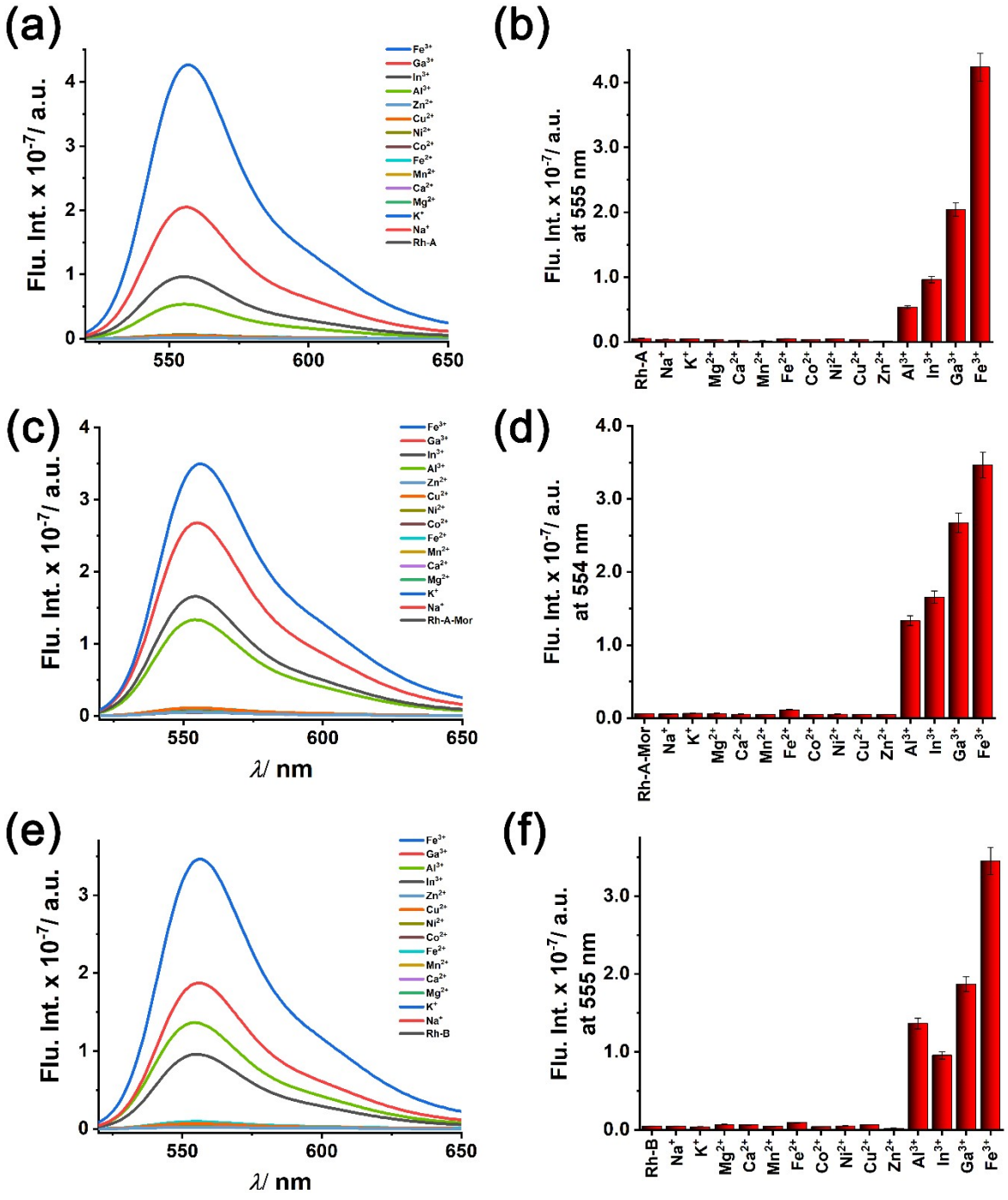

Fig. S18: Emission-based metal ion selectivity studies. Fluorescence spectra and emission maxima bar plots of 10 μM **Rh-A (a, b)**, **Rh-A-Mor (c, d)**, and **Rh-B (e, f)** upon addition of metal ions (50 μM) of Na^+, K^+, Mg^{2+}, Ca^{2+}, Mn^{2+}, Fe^{2+}, Co^{2+}, Ni^{2+}, Cu^{2+}, Zn^{2+}, Al^{3+}, In^{3+}, Ga^{3+} and Fe^{3+} in NaCl solution (ionic strength 20 mM, pH 6.0, 37 °C), λ_{ex} = 510 nm.

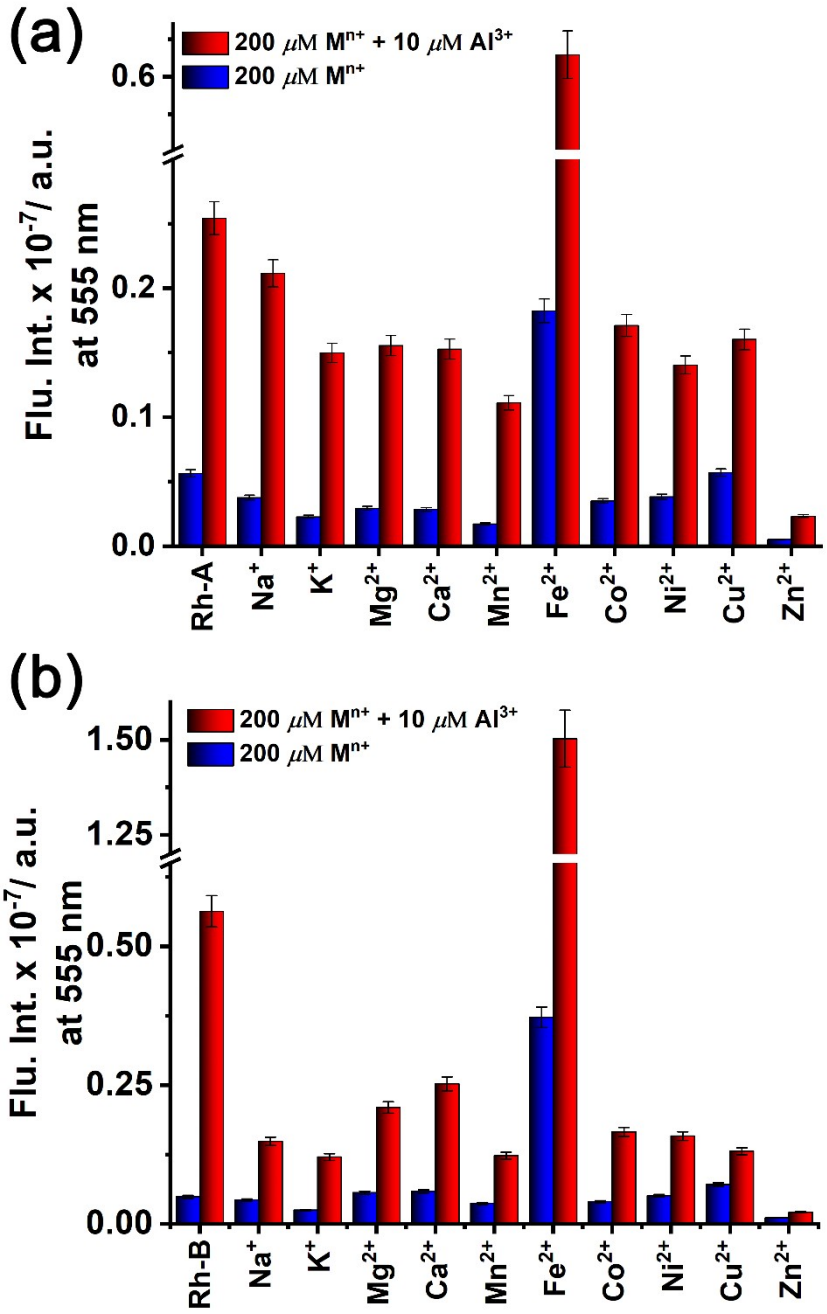

Fig. S19: Selectivity studies of (a) **Rh-A and (b) Rh-B** in presence of other biologically relevant mono and divalent metal ions (200 μM) and Al^{3+} (10 μM) in NaCl solution (ionic strength 20 mM, pH 6.0, 37 °C), [**Rh-A**] = [**Rh-B**] = 10 μM, λ_{ex} = 510 nm.

Selectivity and interference studies

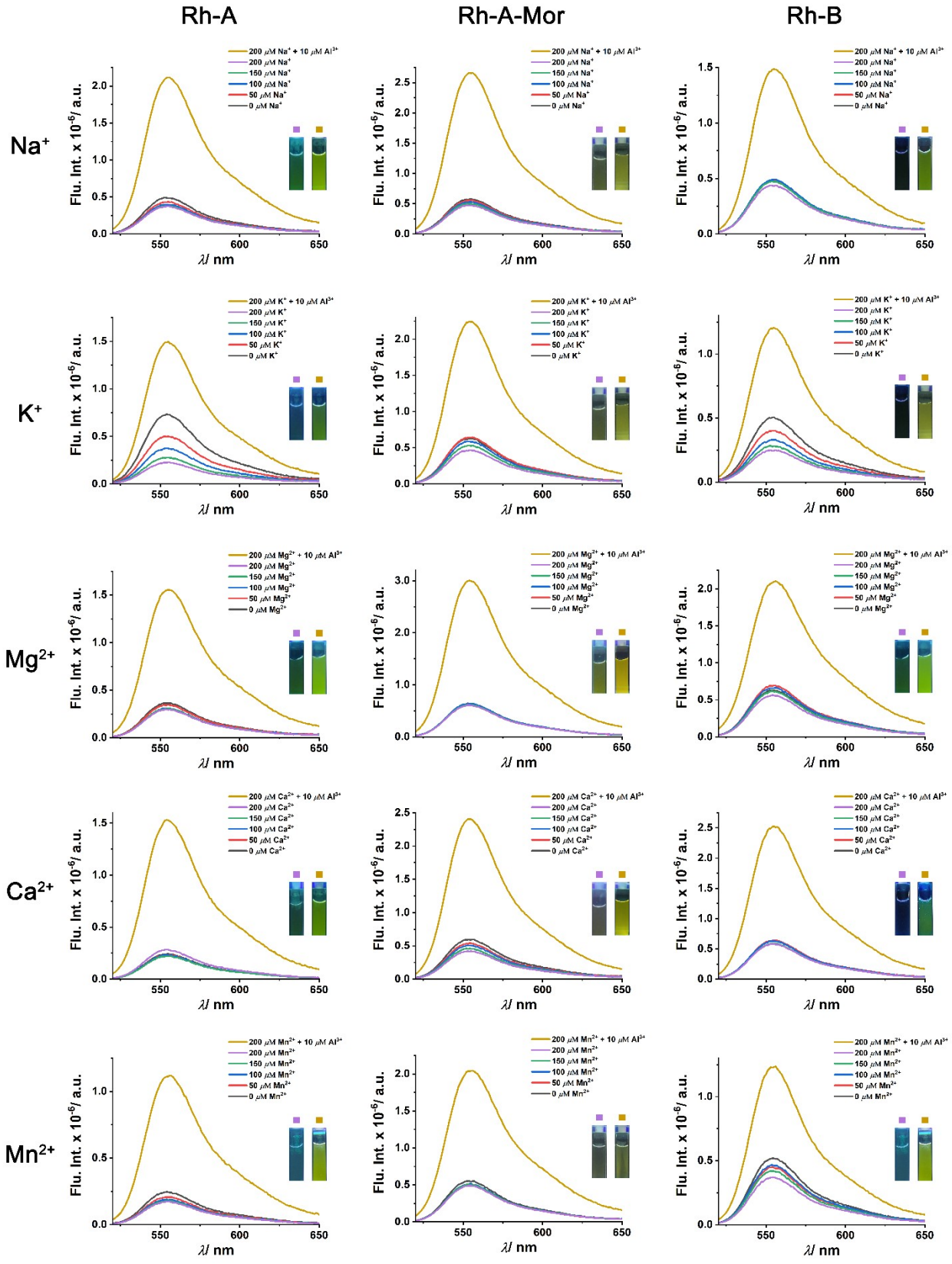

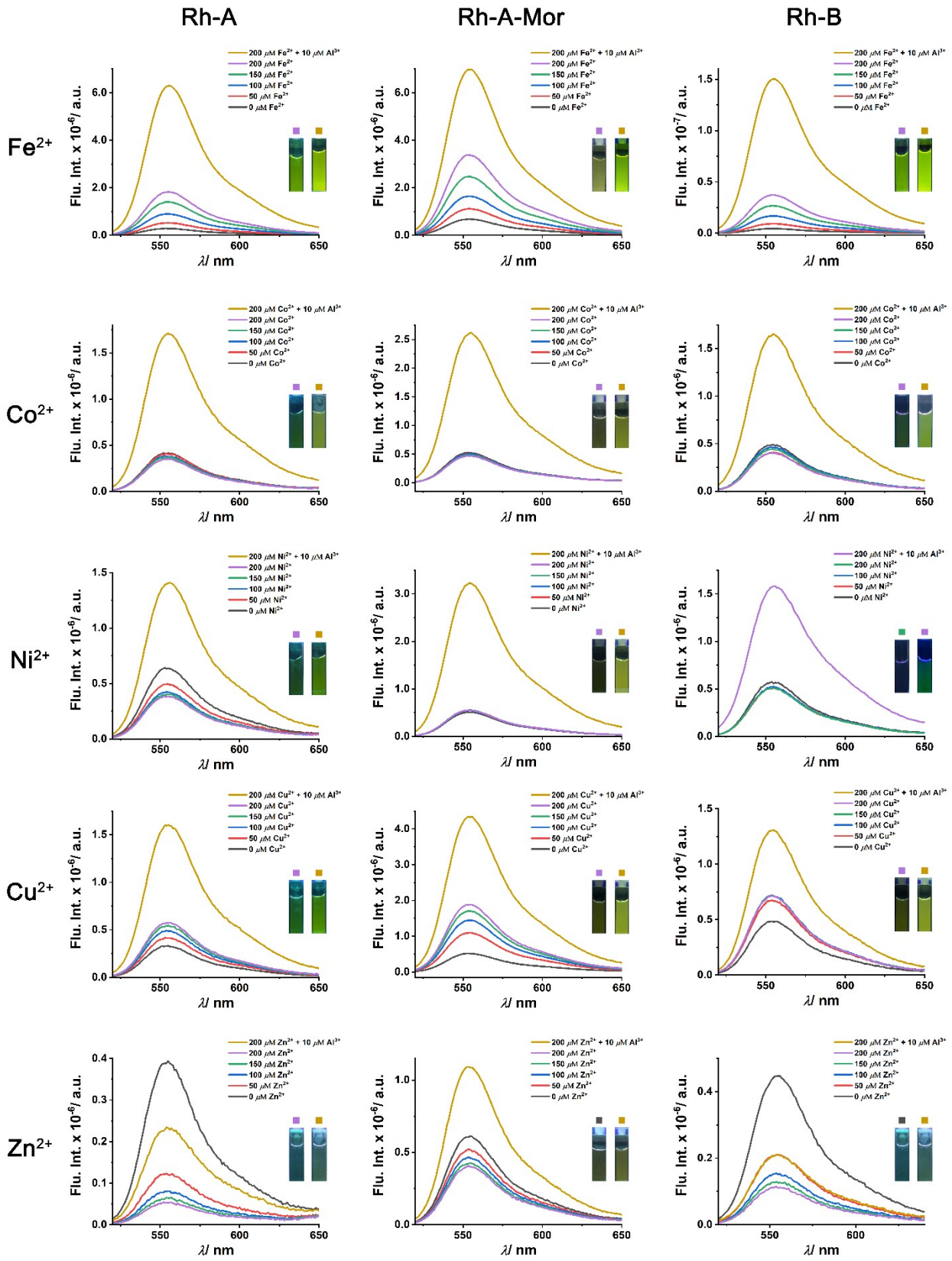

Fig. S20: Selectivity and interference plots of chemosensors with individual mono and bivalent metal ions. The squares represent the spectra corresponding to the cuvette images.

Table S2: Binding constants (K) and limit of detection (LOD) of Al^{3+} sensors from steady-state absorption and emission studies.

Chemosensor	K/ M^{-1}		LOD/ μM	
	Emission studies	Absorption studies	Emission studies	Absorption studies
Rh-A	$(1.69 \pm 0.19) \times 10^4$	$(1.74 \pm 0.13) \times 10^4$	0.13	0.45
Rh-A-Mor	$(3.22 \pm 0.20) \times 10^4$	$(4.13 \pm 0.27) \times 10^4$	0.10	0.21
Rh-B	$(2.10 \pm 0.13) \times 10^4$	$(1.10 \pm 0.05) \times 10^4$	0.17	0.40

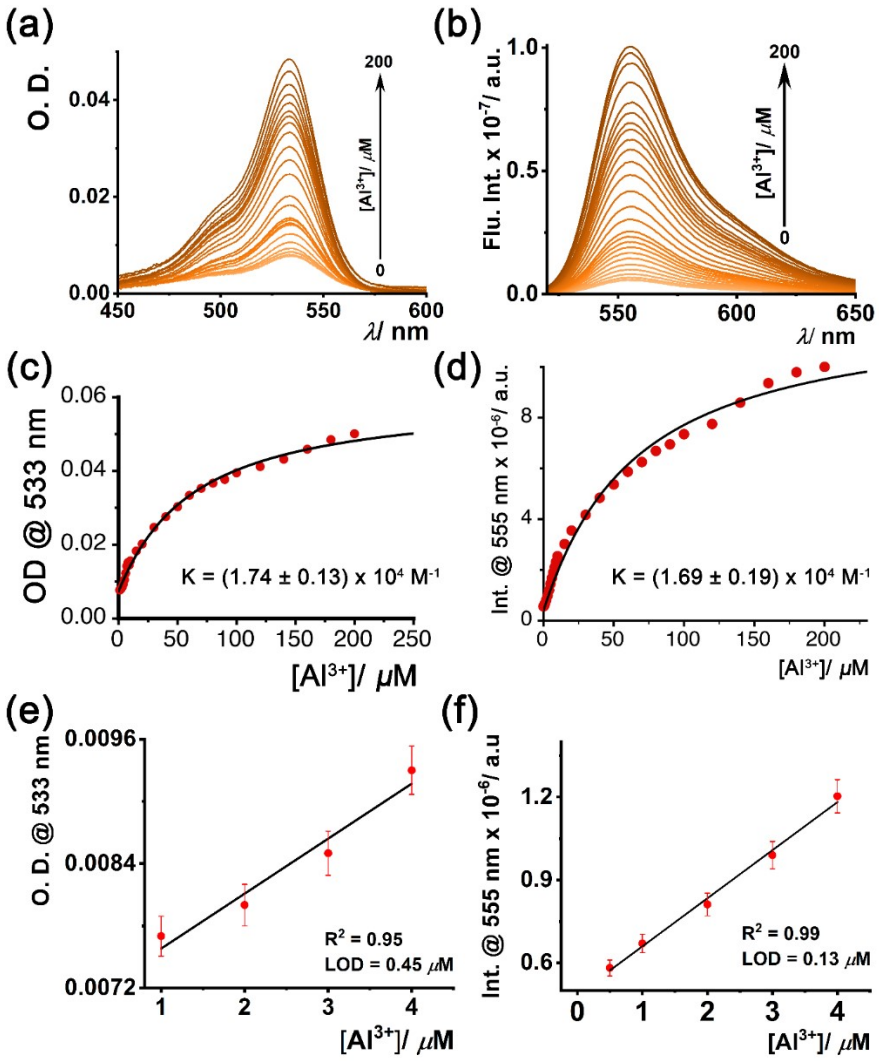

Fig. S21: (a) and (b) shows the UV-Vis. absorption and emission spectra of **Rh-A** (10 μM) in presence of Al^{3+} (0-200 μM), (c) and (d) are the binding plots of **Rh-A** with [Al^{3+}] obtained from UV-Vis. absorption and emission spectra respectively, according to the 1:1 fitting

equation, LOD obtained from (e) UV-Vis. absorption and (f) emission spectra of **Rh-A** with increasing concentration of Al^{3+}, all the experiments are performed using NaCl solution (ionic strength 20 mM, pH 6.0, 37 °C), [**Rh-A**] = 10 μM, λ_{ex} = 510 nm.

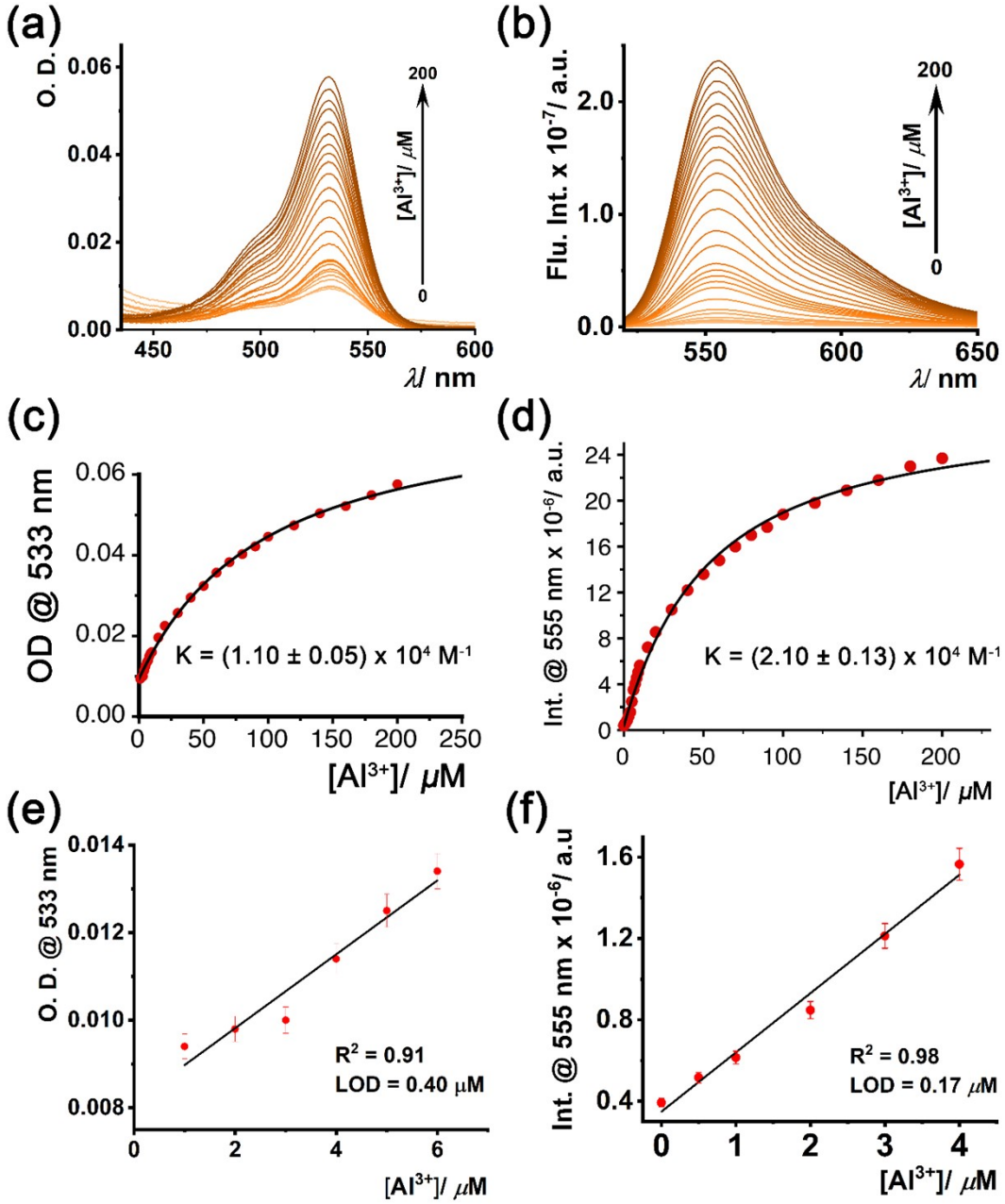

Fig. S22: (a) and (b) shows the UV-Vis. absorption and emission spectra of **Rh-B** (10 μM) in presence of Al^{3+} (0-200 μM), (c) and (d) are the binding plots of **Rh-B** with [Al^{3+}] obtained from UV-Vis. absorption and emission spectra respectively, according to the 1:1 fitting equation, LOD obtained from (e) UV-Vis. absorption and (f) emission spectra of **Rh-B** with increasing concentration of Al^{3+}, all the experiments are performed using NaCl solution (ionic strength 20 mM, pH 6.0, 37 °C), [**Rh-B**] = 10 μM, λ_{ex} = 510 nm.

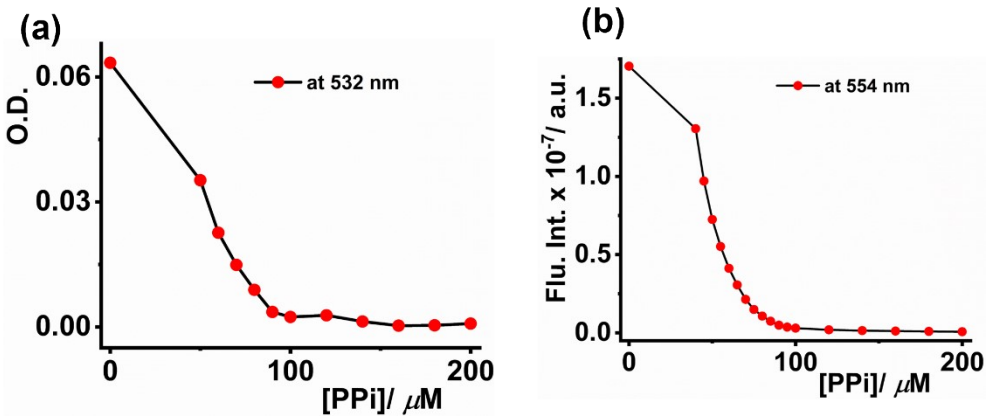

Fig. S23: (a) and (b) represent the plot of absorption and emission of Al^{3+} (100 μM) complexes of **Rh-A-Mor** as a function of [PPi] at 532 nm and 554 nm respectively, all experiments performed in NaCl solution (ionic strength 20 mM, pH 6.0, 37 ℃).

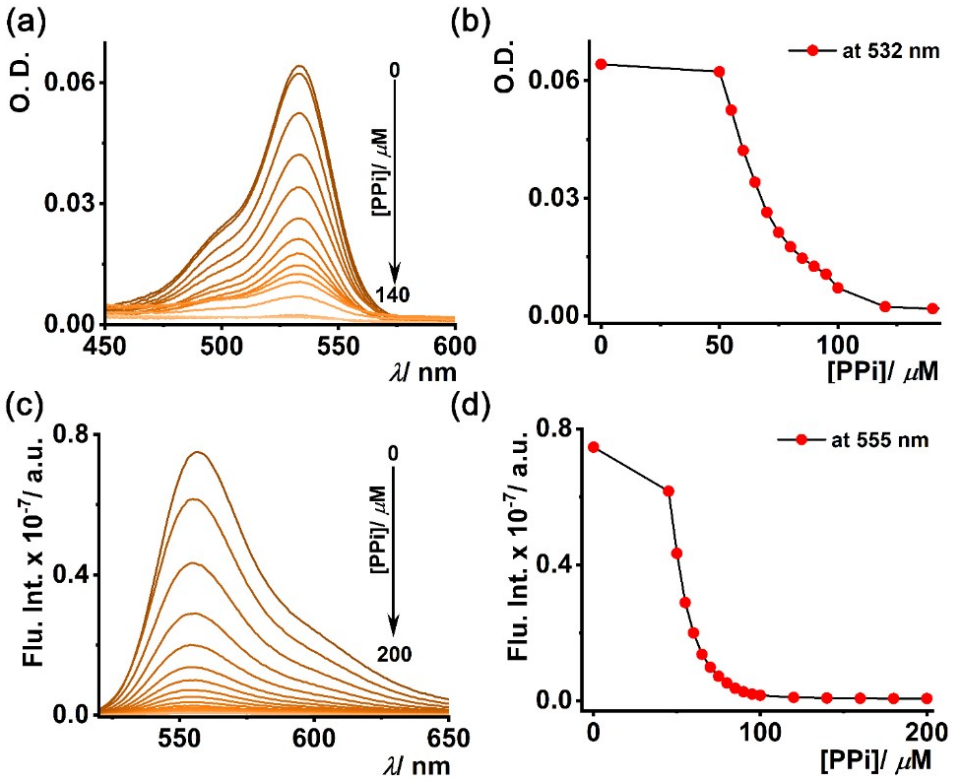

Fig. S24: (a) UV-Vis. absorption and (c) emission spectra of Al^{3+} (100 μM) complexes of **Rh-A** upon PPi addition, (b) and (d) represent the plot of absorption and emission as a function of [PPi] at 532 nm and 555 nm respectively, all experiments performed in NaCl solution (ionic strength 20 mM, pH 6.0, 37 ℃).

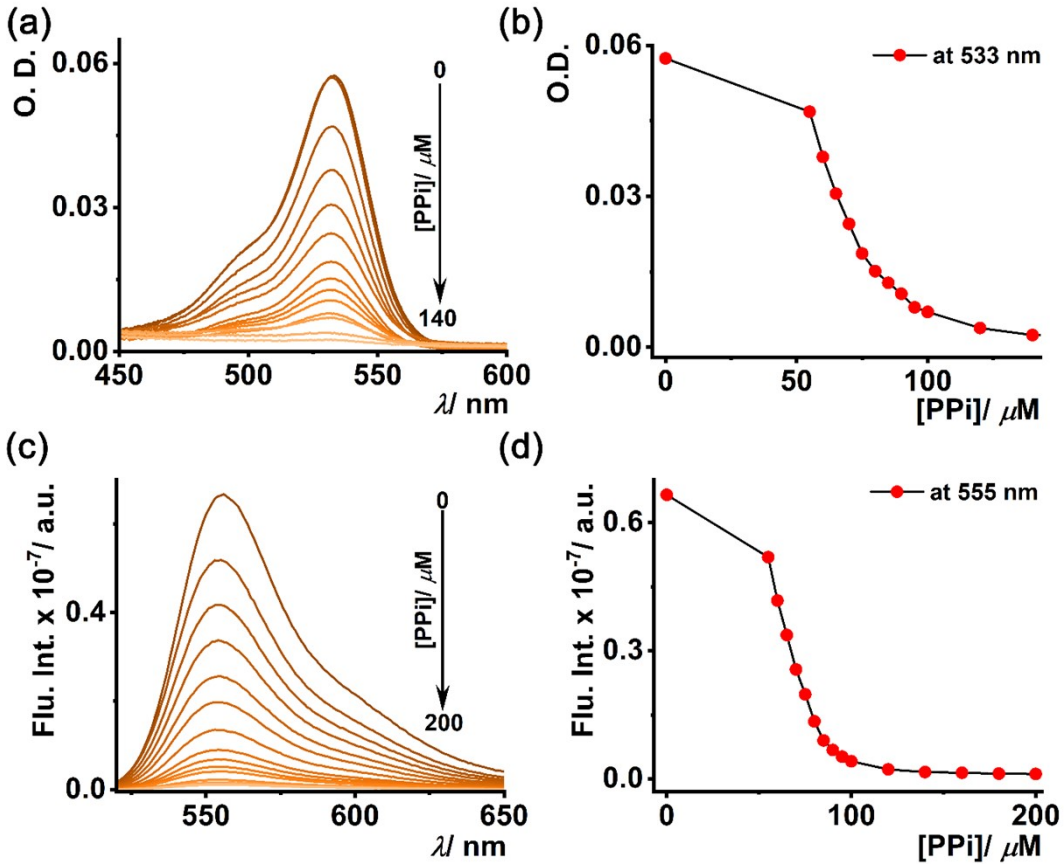

Fig. S25: (a) UV-Vis. absorption and (c) emission spectra of Al^{3+} (100 μM) complexes of **Rh-B** upon PPi addition, (b) and (d) represent the plot of absorption and emission as a function of [PPi] at 533 nm and 555 nm respectively, all experiments performed in NaCl solution (ionic strength 20 mM, pH 6.0, 37 ℃).

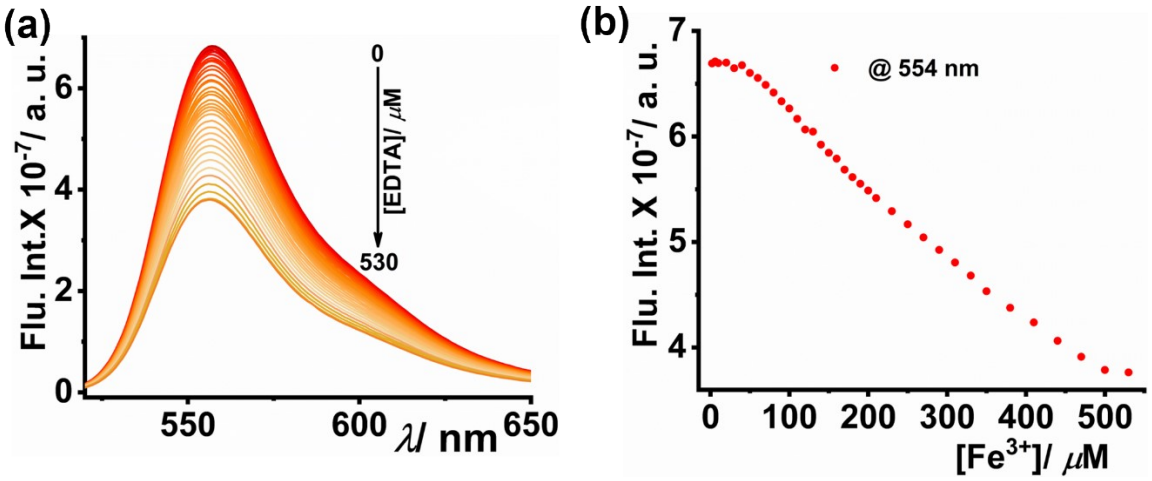

Fig. S26: Emission spectra of Fe^{3+} complex of **Rh-A-Mor** (5 μM) upon EDTA addition, (b) represent the plot of emission as a function of EDTA concentration at 554 nm, all experiments performed in NaCl solution (ionic strength 20 mM, pH 6.0, 37 ℃).

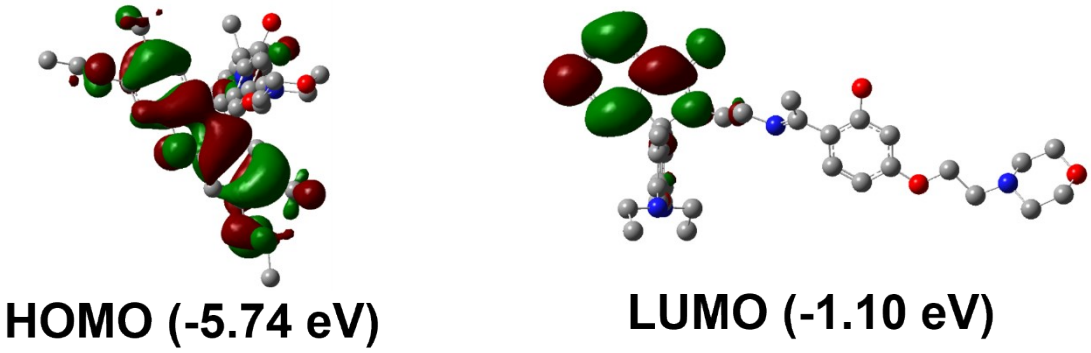

Fig. S27: Electron density plots of the dominating frontier molecular orbitals which are involved in the major electronic transitions in **Rh-A-Mor** (closed)

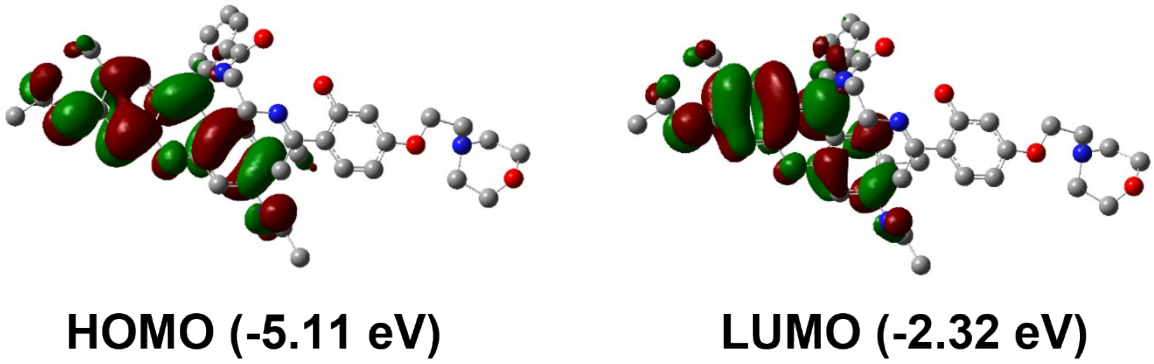

Fig. S28: Electron density plots of the dominating frontier molecular orbitals which are involved in the major electronic transitions in **Rh-A-Mor** (open)

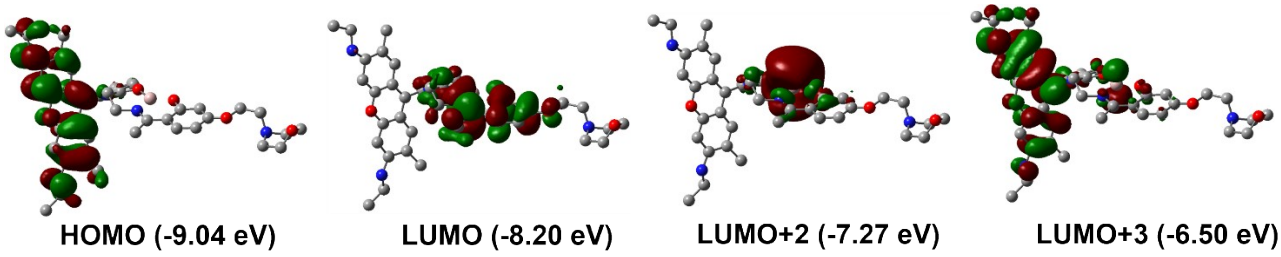

Fig. S29: Electron density plots of the dominating frontier molecular orbitals which are involved in the major electronic transitions in **Rh-A-Mor**-Al^{3+}

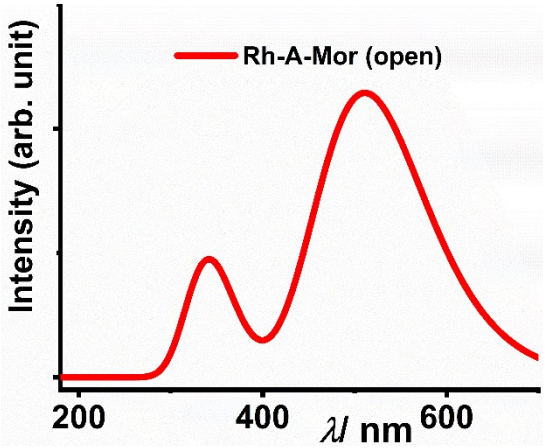

Fig. S30: Simulated emission spectra of **Rh-A-Mor** (open)

Table S30: Absorption characteristics of **Rh-A-Mor** and Rh-A-Mor-Al^{3+} complex, showing the nature of electronic transitions.

Species	λ_{max} in nm (oscillator strength)	Involved MOs (% of CI)	Transition characteristics
Rh-A-Mor (closed)	256 (0.39) 223 (0.61) 210 (0.52)	H-1→L+1 (46), H-1 →L+2 (25) H→L+3 (26), H-2 →L+1 (14), H-2 →L+2 (15) More complicated	π-π* π-π*
Rh-A-Mor (open)	423 (0.70) 259 (0.40)	H→L (95) H→L+3 (35), H-6 →L (23)	π-π* π-π*
Rh-A-Mor-Al^{3+}	465 (0.51)	H→L+3 (65), H →L+2 (26)	π-π* + LMCT

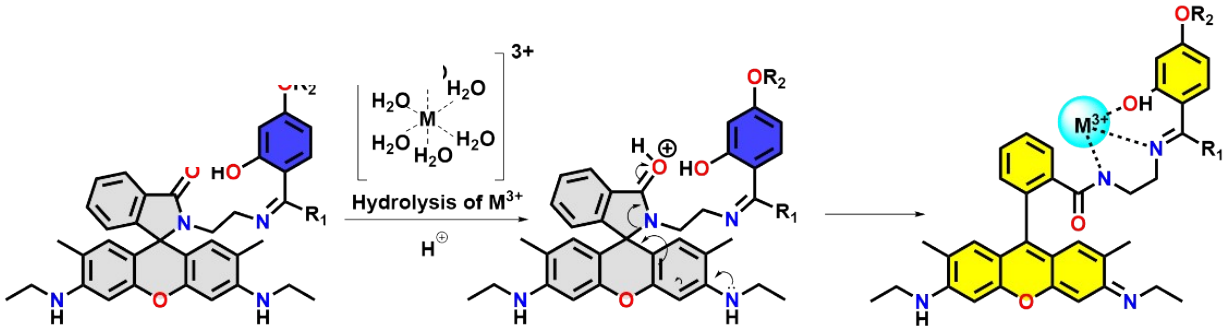

Scheme S2: Mechanism of hydrolysis-driven ring opening of spirolactam form and turn-on response with tri-valent metal ions.

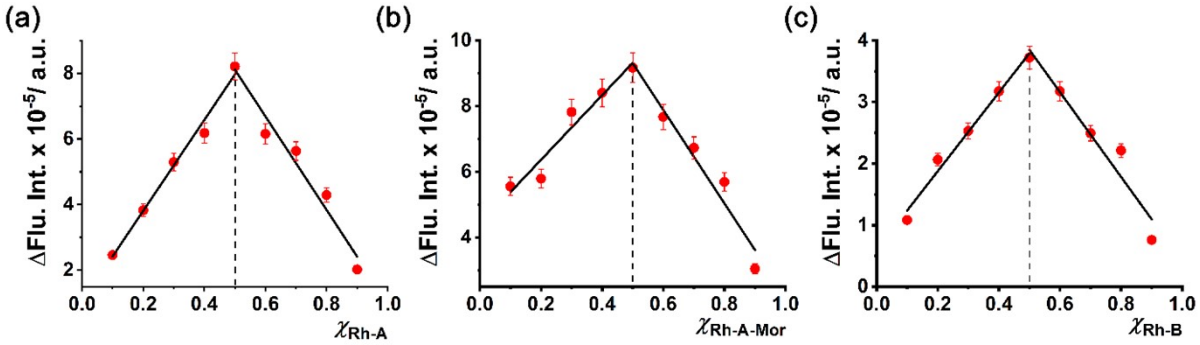

Fig. S31: Job's plot for (a) **Rh-A**, (b) **Rh-A-Mor**, (c) **Rh-B**

4. NMR titration with Al^{3+} and PPi

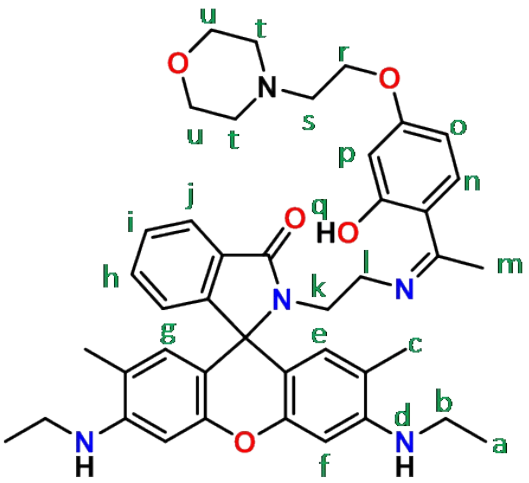

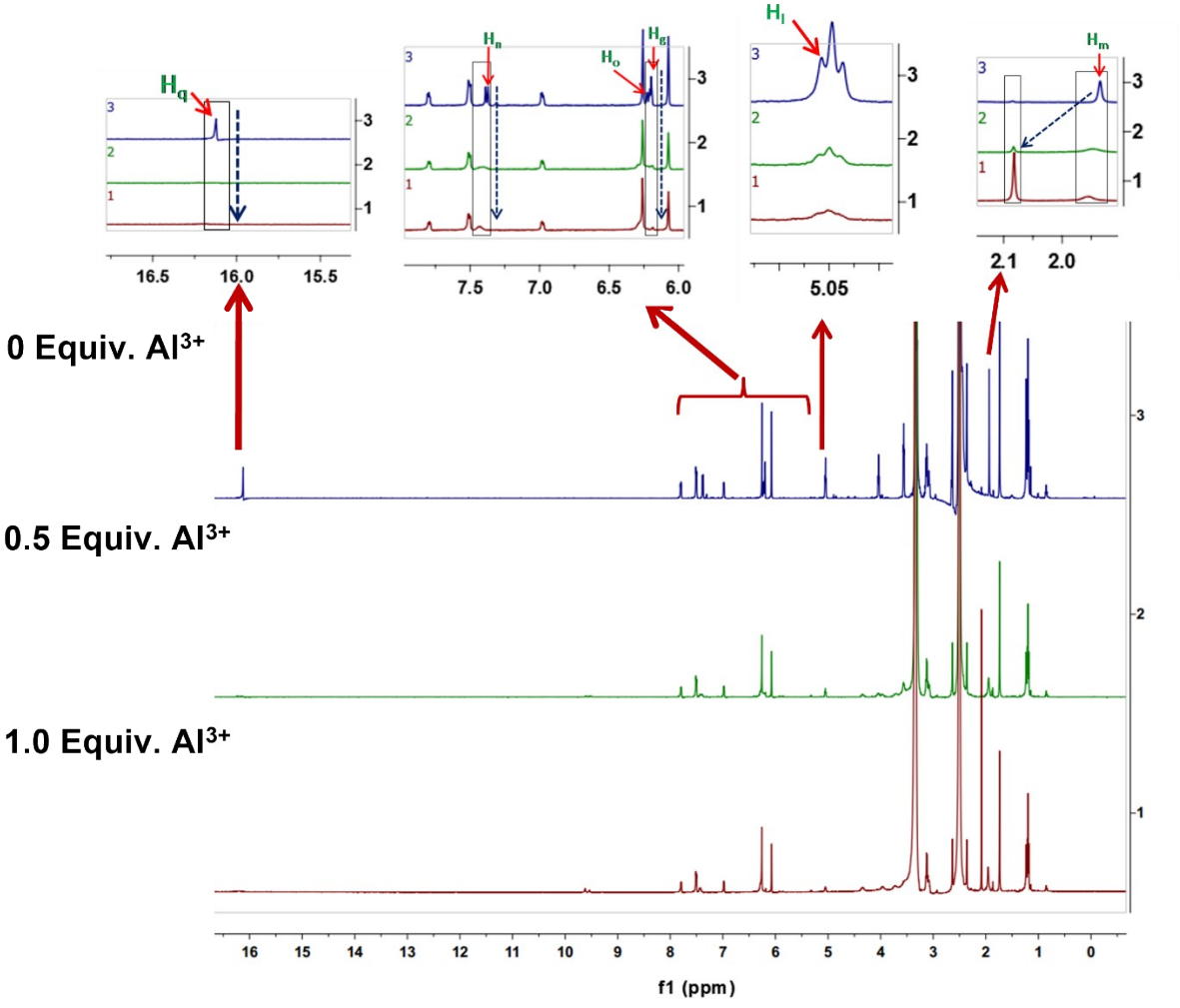

Fig. S32: ^{1}H NMR titration of **Rh-A-Mor** with 0, 0.5, and 1 equivalent of Al^{3+} in DMSO-d6.

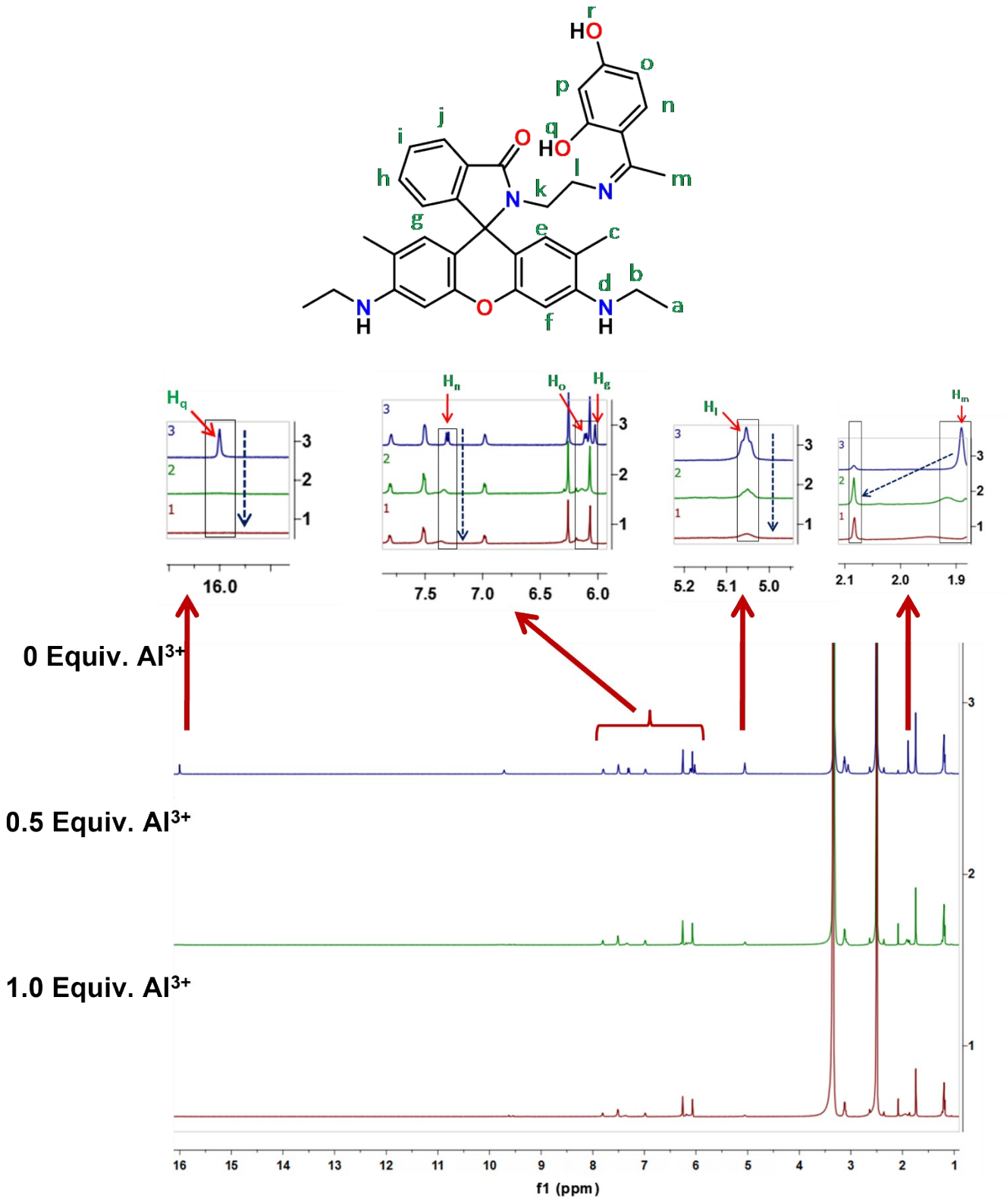

Fig. S33: ^{1}H NMR titration of **Rh-A** with 0, 0.5, and 1 equivalent of Al^{3+} in DMSO-d6.

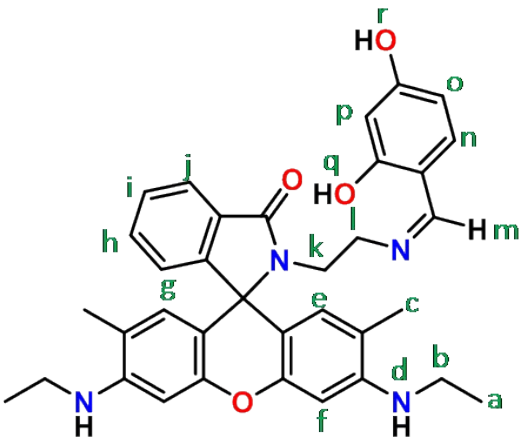

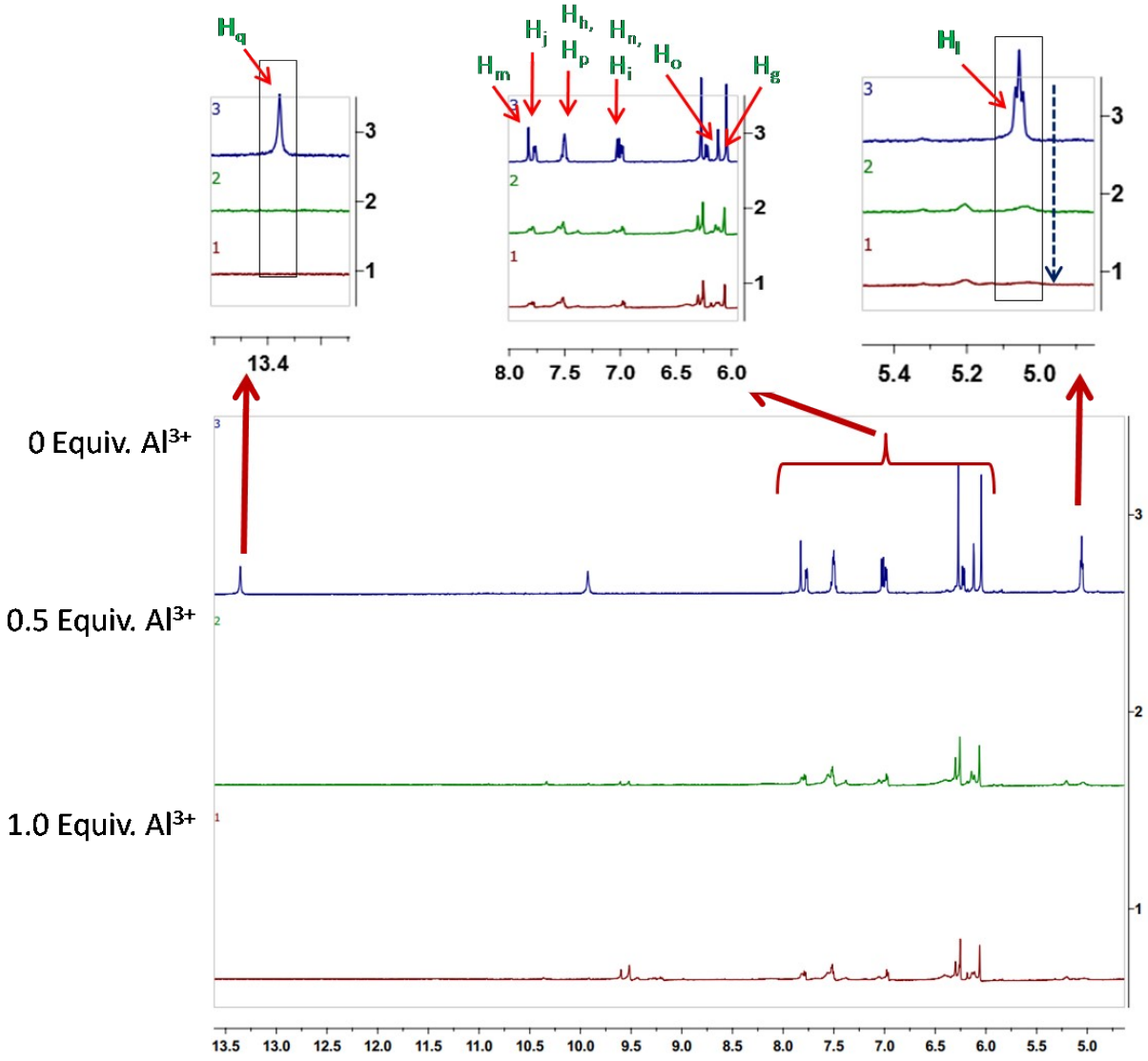

Fig. S34: ^{1}H NMR titration of **Rh-B** with 0, 0.5, and 1 equivalent of Al^{3+} in DMSO-d6.

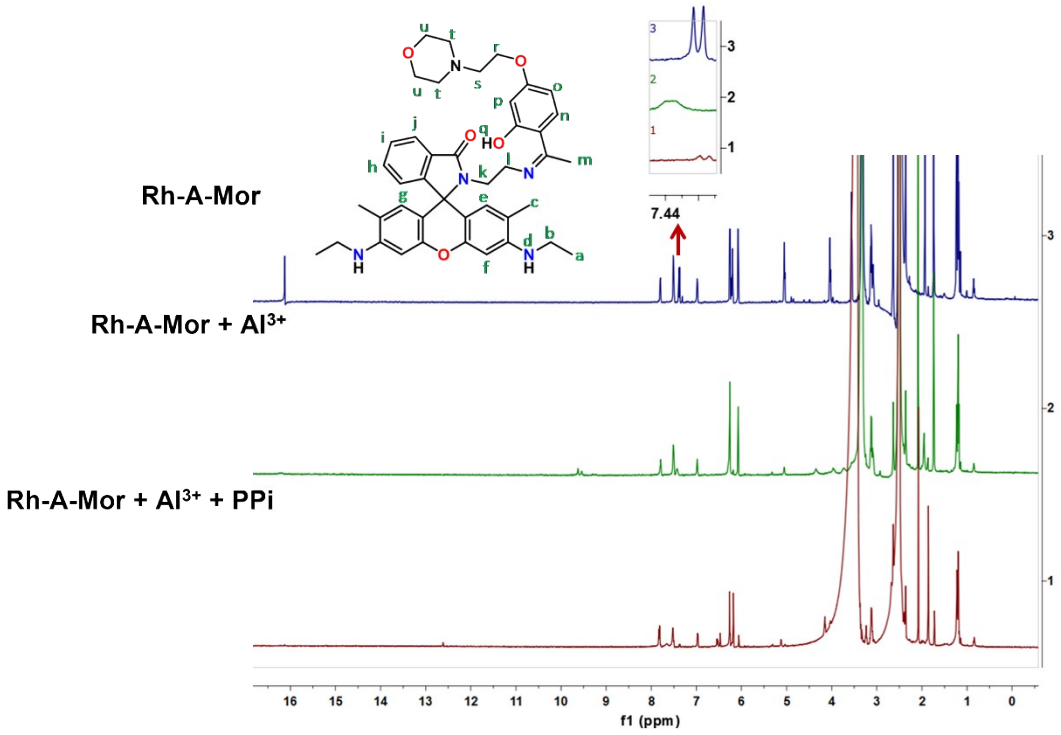

Fig. S35: ^{1}H NMR titration of **Rh-A-Mor** with Al^{3+} and PPi

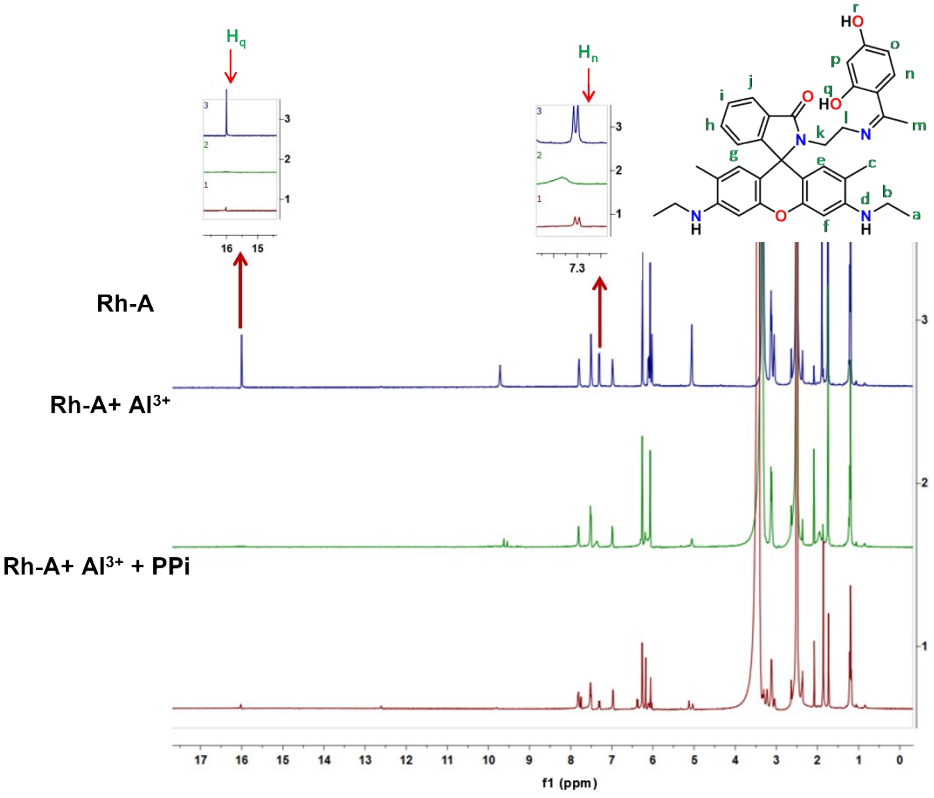

Fig. S36: ^{1}H NMR titration of **Rh-A** with Al^{3+} and PPi

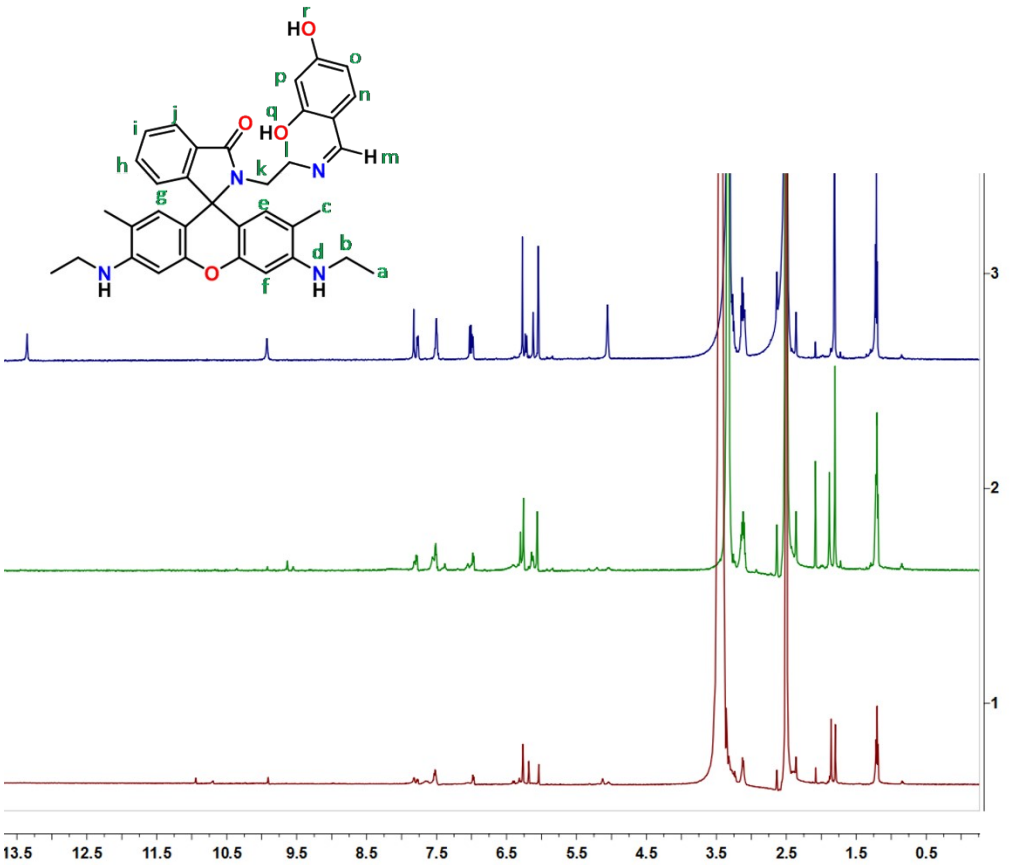

Fig. S37: ^{1}H NMR titration of **Rh-B** with Al^{3+} and PPi

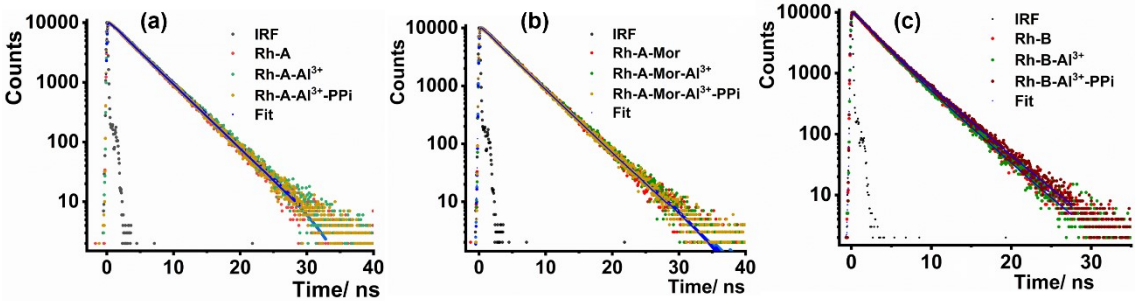

(d)

	Compound Name	Lifetime/ ns	Compound Name	Lifetime/ ns	Compound Name	Lifetime/ ns
1	Rh-A	3.9	Rh-A-Mor	3.8	Rh-B	3.2
2	Rh-A-Al^{3+}	4.0	Rh-A-Mor-Al^{3+}	3.8	Rh-B-Al^{3+}	3.2
3	Rh-A-Al^{3+}-PPi	3.9	Rh-A-Mor-Al^{3+}-PPi	3.8	Rh-B-Al^{3+}-PPi	3.4

Fig. S38: Fluorescence lifetime decay of (a) Rh-A, Rh-A-Al^{3+}, and Rh-A-Al^{3+}-PPi, (b) Rh-A-mor, Rh-A-Mor- Al^{3+}, Rh-A-Mor-Al^{3+}-PPi, (c) Rh-B, Rh-B- Al^{3+}, Rh-B-Al^{3+}-PPi, and (d) lifetime values of Rh derivatives in different conditions.

5. Live-cell imaging studies:

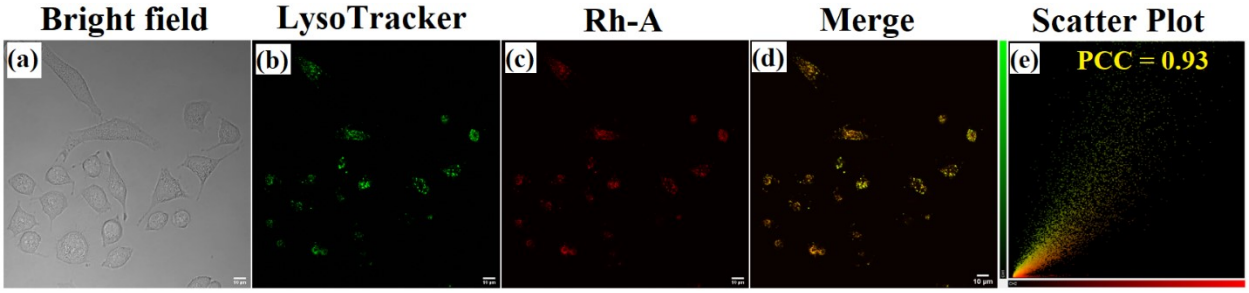

Fig. S39: Confocal fluorescence microscopic images of HeLa cells co-stained with 300 nM LysoTracker green and 1 μM **Rh-A** for 10 min at 37 °C. Images represent (a) Bright field, (b) fluorescence from LysoTracker green (λ_{ex}= 488 nm, λ_{em} = 500-540 nm), (c) fluorescence from **Rh-A** (λ_{ex} = 561 nm, λ_{em} = 570-670 nm), (d) merge image of b and c, and (e) Scatter plot showing Pearson's correlation coefficient of 0.93 ± 0.01. (Scale bar = 10 μm)

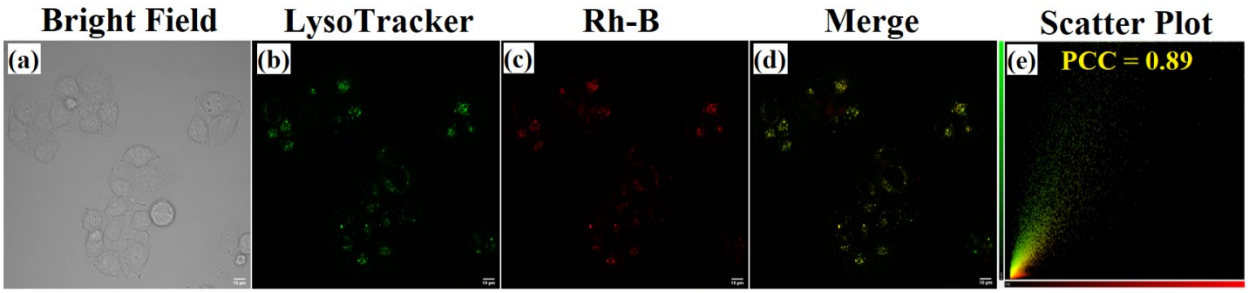

Fig. S40: Confocal fluorescence microscopic images of HeLa cells co-stained with 300 nM LysoTracker green and 1 μM **Rh-B** for 10 min at 37 °C. Images represent (a) Bright field, (b) fluorescence from LysoTracker green (λ_{ex}= 488 nm, λ_{em} = 500-540 nm), (c) fluorescence from **Rh-B** (λ_{ex} = 561 nm, λ_{em} = 570-670 nm), (d) merge image of b and c, and (e) Scatter plot showing Pearson's correlation coefficient of 0.89 ± 0.01. (Scale bar = 10 μm).

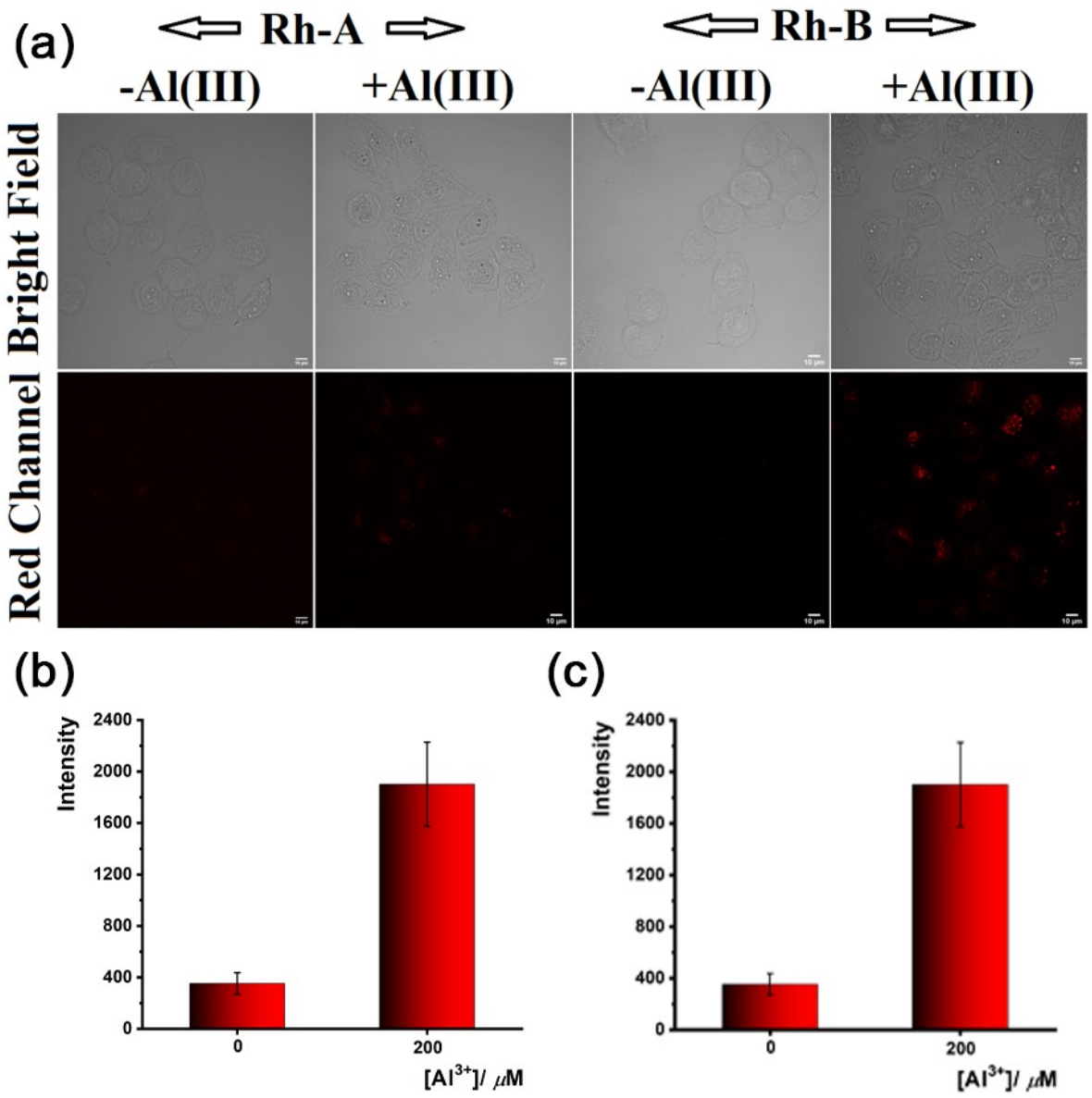

Fig. S41: (a) Confocal fluorescence microscopic images of HeLa cells pretreated with 1 μM **Rh-A** and **Rh-B** for 10 mins and then treated with and without Al^{3+} for 15 mins (λ_{ex} = 561 nm, λ_{em} = 570-670 nm), (b) and (c) quantitative analysis of the fluorescence intensity of (a). Scale bar = 10 μm

6. References

1. Soh, J. H.; Swamy, K.; Kim, S. K.; Kim, S.; Lee, S.-H.; Yoon, J. Rhodamine urea derivatives as fluorescent chemosensors for Hg^{2+}. *Tetrahedron Lett* **2007**, *34* (48), 5966–5969.

2. Roma, G.; Di Braccio, M.; Grossi, G.; Piras, D.; Leoncini, G.; Bruzzese, D.; Signorello, M. G.; Fossa, P.; Mosti, L., Synthesis and in vitro antiplatelet activity of new 4-(1-piperazinyl)coumarin derivatives. Human platelet phosphodiesterase 3 inhibitory properties of the two most effective compounds described and molecular modeling study on their interactions with phosphodiesterase 3A catalytic site. *J. Med. Chem.* **2007,** *50* (12), 2886-2895.